UNIVERSITY RESEARCH PROGRAM IN ROBOTICS

Robotics Technology Development Program

Grant No.: DE-FG52-04NA25588/A001

FINAL TECHNICAL ANNUAL REPORT

Project Period: 9/1/06 – 8/31/07

Investigators

James S. Tulenko – P.I.

tulenko@ufl.edu

Carl D. Crane, III – Co-P.I.

ccrane@ufl.edu

UF | UNIVERSITY of FLORIDA

College of Engineering

Nuclear & Radiological Engineering and Mechanical & Aero Engineering

P.O. Box 118300, Gainesville, FL, 32611-8300

(352) 392-1401 or (352) 392-9461

Table of Contents

Research Team Personnel

A. Principal Faculty	**B. Associated Faculty**	**C. Post-Doctoral & Sub Faculty**
Dr. Carl D. Crane III	Dr. David Hintenlang	Dr. Dean Schoenfeld
Prof. James S. Tulenko		

D. Students Graduated:

Julio Correa, Ph.D.

Javier Roldan McKinley, PhD.

E. Students Supported:

Antoin Baker, PhD.

Ryan Fisher, M.S.

William E. Maloney, M.S.

Roberto Montane, PhD.

Jose Santiago, Ph.D.

Vishesh Vikas, M.S

Jean-Francois Kamath, PhD.

Publications & Reports Issued

- *"Survivable Mobile Robot System with Multi-Task Capabilities,"* Schoenfeld, D., Tulenko, J. A., Dept. of Nuclear & Radiological Engineering, University of Florida, Gainesville, FL, Sharing Solutions for Emergencies and Hazardous Environments, ANS Salt Lake City, UT, February 2006.

- *"An Improved Integrated Rad-Hard Wireless Communication/Control System With Dual Use Applications,"* Schoenfeld, D., Kurtz, J., Carlson, P., Tulenko, J. A., Dept. of Nuclear & Radiological Engineering, University of Florida, Gainesville, FL, Sharing Solutions for Emergencies and Hazardous Environments, ANS, Salt Lake City, UT, February 2006.

- *"Processing of clinical images for guidance of robotic assisted procedures,"* D.E. Hintenlang, Dept. of Nuclear & Radiological Engineering, University of Florida, Gainesville, FL, 10th International Conference on Robotics and Remote Systems for Hazardous Environments, 405-410, Gainesville, FL, March 2006.

- ***"****3-D Visualization of MEMS using Micro-CT,"* D. E. Hintenlang, R. Fisher, W. Moloney, Dept. of Nuclear & Radiological Engineering, University of Florida, Gainesville, FL, Future Technologies Conference II, Sponsored by the National Nuclear Security Administration, Hyatt Regency Washington, Washington, DC, October 2006

- "*Development of Active and Passive Mechanisms to Control Contact Forces During In-Contact Operations,"* C. D. Crane III, S. Ridgeway, Jean-Francois Kamath, Center for Intelligent Machines and Robotics, University of Florida, Gainesville, FL, Future Technologies Conference II, Sponsored by the National Nuclear Security Administration, Hyatt Regency Washington, Washington, DC, October 2006

- *"Nano-Power Source Designs For Future MEMS and Sensor Applications,"* D. W. Schoenfeld and J.S. Tulenko, University of Florida, Nuclear and Radiological Engineering, Gainesville, FL, W. V. Schoenfeld, University of Central Florida, CREOL-College of Optics & Photonics, Orlando, FL, and A. L. Huston, Naval Research Laboratory, Command Support Division, Washington, D.C., Future Technologies Conference II, Sponsored by the National Nuclear Security Administration, Hyatt Regency Washington, Wash., DC, Oct. 2006

- "*Static Analysis of Tensegrity Structures,"* Crane, C., Duffy, J. and Correa, J., 2006, Journal of Mechanical Design, **127**(2), pp. 257-268.

Terms & Acronyms

B.R.	Branching Ratio
CMOS	Complementary Metal Oxide Semi-Conductor
COTS	Commercial off-the-shelf
CNR	Contrast-to-noise Ratio
CSDA	Continuous slowing down approximation
DmTS	Digital micro-Tomosynthesis
GaAs	Gallium Arsenide
GaN	Gallium Nitride
GPIP Bus	General Purpose Interface Bus
JFET	Junction Field Effect Transistor
LMS	Laser Measuring System
LIGA	Microtechnology for manuf'g. high-aspect-ratio structures
MEMS	Micro-Electro-Mechanical System
MOS	Metal oxide semiconductor dosimeters (also radfets)
MOSFETs	Metal-Oxide Semiconductor Field-Effect-Transistors
MOT	metal-oxide technology
MPa	Mega-Pascal
NDE	Non-destructive Examination
PCCFC	Parallel Compliant Coupler for Force Control
PECVD	Plasma enhanced chemical vapor deposition
Quadrature	Compare two wave forms of differing phases
Quantized	Subdivided into small, measurable increments
RADFET	Solid State Radiation Dosimeter Field-Effect-Transistors
SEM	Scanning Electron Microscope
SOI	Silicon on insulator
Tensegrity	Contraction of tension and integrity
WCPMMI	Weight Compensating Parallel Manipulator/Manual Input

1.0 Development of Nano-Scale Radioisotope Battery Models and Supporting Radiation Testing of Components

1.1 Objective:

The objective for the FY06/07 fiscal year is the development of nano-scale radioisotope powered battery models and supporting radiation testing of components.

1.2 Task & Accomplishments

This task focuses on the concepts of conversion technologies for radioisotope battery designs and the further investigation of radiation resilience levels of candidate materials identified during FY06 and FY07 for fluorescence or 'direct' generation of free current electrons in transducers. Physical testing of key energy conversion parameters were initiated and carried out in order to augment MCNP and the EGS transport code programs and provide the realistic insights to improvements in design of nano-scale radioisotope battery design. In FY07 such advances in design are being computationally pretested via MCNP and EGS and with semi-analytical formulations (when appropriate).

The UF development and design team continues the development of a nano-scale radioisotope battery designs and design schemes that have the potential to provide sufficient power for MEMS devices under development in cutting edge laboratories in the US. Studies of fundamental mechanisms and simulation studies of stacked tandem cells optimized for indirect conversion have led to the design concept of using super-1 kilo-eV induced fluorescence of dielectric layers with transparent photovoltaic conversion devices. For all of our materials, fluorescence and phosphorescence overlap in their function. While many standard phosphors typically provide higher conversion ratios, radiation damage from most radioisotopes quickly degrade this initial advantage for power conversion. Reported progress in the radiation tolerance of phosphorescent materials has provided relevant examples and important guidance. There is such supporting progress reported from research by A. L. Huston, B. L. Justus and co-workers at the Optical Sciences Division, Naval Research Laboratory, 4555 Overlook Avenue, SW, Washington, D.C. on Cu^{1+}-doped glass. [1]. Fabrication and experimental testing of Cu^{1+}-doped glass provides a technology compatible with the semiconductor processing technology required by tandem cell designs. Simulations via MCNP5, EGS, MCNPX (mcnpx for α's) of absorption of kinetic energy of beta particles and alpha particles by the microscopic material medium consisting of appropriate strata of materials to have transducing (or transducer-based) performances infer a realistic but occasionally modest capability for power production by indirect energy conversion mechanisms. However, indirect conversion of light produced from appropriate radiative energy dissipating materials is supported by advanced photovoltaic devices with micron or sub-micron geometries and robust conversion efficiencies (10-40%).

1.2.2 Design of Nuclear Batteries for Micro and Nano-Scale

Betavoltaic designs and indirect conversion designs appear to overcome many of the problems of the repulsive field effect within a capacitive direct conversion device when the dimensions of the empty gap or stratum of medium of dissipating energy conversion is not much larger than 1/2 of the range of the average beta or alpha particle of the fuel source. This empty gap or stratum of energy conversion surrounds the fuel source. A beta-powered capacitive conversion device is basically a capacitor which functions as a battery in which the fuel source is the beta

particle cathode and a cylindrical shell or other sheath remotely surrounds the fuel. See ref. [2] for detailed description of a capacitive direct conversion device. The capacitive direct energy conversion device has been discussed here mainly in order to contrast its disadvantage in excessive size to betavoltaic designs and indirect conversion designs, which can be compacted roughly to the scales of range of beta or alpha particles. It is explained in ref. [2] that capacitive nuclear batteries need to exceed 1 cm in diameter when using tritium, Ni-63, or any other radioisotopic fuel. Any such battery which is smaller than 1 cm is doomed to electrical efficiency below 1 percent.

There are two worthwhile avenues of development of microscopic and submicroscopic configuration of nuclear batteries which we are pursuing: (M1) development of a beta-voltaic cell and (M2) development of tertiary energy conversion devices which include fluorescence or luminescence for the intermediate conversion of the kinetic energy of secondary electrons, β's, and α's. Note that tertiary energy conversion and intermediate conversion fall under indirect conversion in accordance of the terminology previously used in previous reports and related presentations.

In support of development of (M1), there has been investigation of SiC as a betavoltaic cell with good initial performance. There has been an advocate of SiC for betavoltaic cells in established circles, owing to its initially high performance [3]. However, the efficiency of diodes constituted primarily of SiC does wane with respect to extended dose. Solid-state modified diamond offers even greater potential as betavoltaic device. Diamond has the almost unique property of self-repair crystal structure due to interstitial displacements from radiation. The challenges to developing diamond based transducers hinge around providing both p-type and n-type junctions for such a diode and providing a good conductive contact between the diamond based transducer and the wire conducting electricity to and from the diode.

In support of (M2), there has been a review of and further experimental testing of the Cu+ doped quartz glass. Cu+ doped quartz glass has demonstrated the generation of green photons in response to exposure to beta particles and even X-rays. Lead doped glass also has this property of fluorescence resulting beta (or α) radiation dose [4]. ZnS and Mn and other materials also serve in this way when doped properly with glass. A more exotic configuration of (M2) is to use Krypton or other noble gas which emits UV light in response to irradiation from beta and/or alpha particles. Use of a solid material such Cu+ doped glass in the more standard configuration of (M2) is easier to construct due to its solid nature. Containing a sufficient amount of Krypton fluorescer mixed with or surrounding a radioisotope such as Tritium is an additional burden contingent to use of this exotic configuration with noble gas. This burden makes Kr-84 mixed with Tritium an unlikely candidate for submicroscopic nuclear batteries.

It is illustrative to explain the components of (M2). A nuclear battery of type (M2) consists essentially of: (C1) the radioisotopic fuel; (C2) a material surrounding fuel which undergoes fluorescence or phosphorescence (in range of yellow thru possibly UV) in response to collisions and ionizing irradiation from radiative particles; and (C3) transducers which absorb visible light and efficiently convert it into electrical energy. It is component (C2), the 'fluorescer', which makes (M2) type of nuclear battery unique. Immediately below, we shall explain performances and results or (C1), the fuel from various candidates for radioisotopes. Then experimental results for Cu+ doped quartz as (C2) and prior scholarly knowledge of solid materials which can serve as (C2) shall be discussed.

1.2.3 Discussion of Choices of Radioisotopes; Investigation of Components

Table 1.1 includes a list of potential candidates for fuel for radioisotopic power generators at the nanoscale, micro-scale, or millimeter scale - at largest. It is very informative to inspect the properties and performance capabilities of the radioisotopes selected as candidates. It is the emitters

of highly energetic beta particles which are not quite as suitable for the nano-scale, but still worthy of consideration for helpful comparisons of proportional performances. Various properties of the radioisotopic candidates are included in Table 1.1. With the exception of Cf-252, only isotopes with half-lives greater than 5 years have been included, for the obvious directive of developing a time enduring battery.

Isotope	Density	Activity/gram	Ci Density	Half-Life	Q-Value	Emission modes
H-3	2.52ee-02 *	4831	121.7	12.33	18.5	β
Ar-42	0.16 *	258.9	41.424	32.9	599.4	β
Ni-63	8.88	56.7	503.50	100.1	66.945	β
Kr-85	0.35 *	391.3	137.09	10.756	687.1	β
Sr-90	2.54	138.1	350.77	28.79	546	β
Cs-137	1.87	86.81	162.33	30.05	1175.63	β
Sm-151	7.52	26.31	197.85	90	76.7	β
Pb-210	11.35	76.32	866.23	22.3	63.5	β
Ac-227	10.07	72.3	728.06	21.775	5021(α), 44.8(β)	α (1.4) & β(98.6) **
U-232	18.95	22.35	423.5	68.9	5413.55	α
Pu-238	19.84	17.12	339.7	87.7	5593.2	α
Pu-241	19.84	103.3	2055.4	14.31	20.82,	β
Cm-244	13.5	80.9	1092.2	18.10	5901.61	α
Cf-250	15.1	109.3	1650.4	13.08	6128.44	α
Cf-252	15.1	536.5	8101.2	2.645	6216.87	α
	g/cm3	Ci/g	Ci/cm3	Years	KeV	Particle

Table 1.1 Properties of Radionuclide Sources for Fuel

* The gases in column 2 are at 100 atmospheres and standard temperature.

** In column 6, the powerful alpha particle decay of Ac-227 cannot be ignored when inspecting Ac-227. The weights of {BR (α), B.R.(β)} are {1.4% , 98.6%} respectively. For α, the initial kinetic energy of the average emitted particle equals the Q-value. For β, the average initial kinetic energy of the emitted particle equals 1/3 of the Q-value.

In Table 1.2, ideal performances and more properties of the selected radionuclides are given. Table 1.2 is a continuation of Table 1.1. The ratio of radiated power (of α or beta) per mass of fuel and the ratio of radiated power per volume of fuel are given. Also the maximum CSDA range is given for the emissions of each of the isotopes. "Sig. γ or x-rays" of column 7 stands for most significant gamma ray or x-ray emitted from the given isotope.

Table 1.2 Performances and Properties of Radionuclide Sources for Fuel

Isotope	Half-Life	Power/ gram	Power density	Range in Si material	Sig. γ or x-ray	Q-Value	Emission modes
H-3	12.33	.176349	.4462ee-02	3.9ee-04	No	18.5	β
Ar-42	32.9	.305906	.04895	.120	No	599.4	β
Ni-63	100.1	.749ee-02	.06648	3.9ee-03	No	66.945	Suspe β
Kr-85	10.756	.52999	.185496	.142	.5MeV, γ	687.1	β
Sr-90	28.79	.14860	.377449	.103	1keV, xray	546	β
Cs-137	30.05	.20138	.376586	.259	.67MeV, γ	1175.63	β
Sm-151	90	.398ee-02	.02993	4.6ee-03	20keV, γ	76.7	β
Pb-210	22.3	.956ee-2	.108533	3.6ee-03	50keV, γ	63.5	β
Ac-227	21.775	.04899	.49336	2.5ee-03	15keV, γ	5021(α), 44.8(β)	α & β, mr
U-232	68.9	19.7326	13.57757	2.6ee-03	60keV, γ	5413.55	α
Pu-238	87.7	.566920	11.24769	2.9ee-03	.1MeV, γ	5593.2	α
Pu-241	14.31	.426ee-02	.084466	4.3ee-04	.15MeV, γ	20.82,	β, mr
Cm-244	18.10	2.82709	38.1657	3.0ee-03	50keV γ	5901.61	α
Cf-250	13.08	3.9649	59.8711	3.2ee-03	50keV γ	6128.44	α
Cf-252	2.645	19.7326	297.962	3.4ee-03	.2MeV γ	6216.87	α
	Years	Watt/g	Watt/cm^3	cm	keV or MeV	keV	particle

The columns in Table 1.2 containing the power per mass, the power density, and the CSDA range of the given isotope are of special interest in considering the performance of nuclear battery containing its fuel on a microscopic mother board or MEMS device. The power ratios are desired to be large. But the CSDA range of emissions from the fuel should be as small as possible out of our set of choices. Moreover, for powering a microscopic mother board or MEMS device, the emission of gamma rays or bremsstrahlung generated x-rays should be less than 30 keV with a frequency ratio, or branching ratio (B.R.) of less than 1%. More abundance of kilo eV photons or harder photons would provide disproportionately larger shielding requirements. Note that 'mr' stands for multimodes of decay from long-lived but unstable daughters of a given isotope in the table. Because these 'mr' decays last for eons, their contribution to power is trivial.

Following with the goal of developing nuclear batteries which power MEMS devices and function durably together with the MEMS devices, we favor the following isotopes: Ni-63, Sm-151, and tritium. Outside of the final stages of this project and for nuclear batteries powering devices which are on the millimeter scale or cm scale occasional emission of harder photons such as 100 keV and predominant emission of α's or β's with greater than 1 or 2 millimeters is acceptable do to more room for placement of components and more room for extra shielding to protect from the harder photons.

In order to follow up the data on alpha particle emitters, one should review and consider some of the results of examples of simulation of radiation dose due to alpha particles from an Ac-227 source. In Figure 1.1, a target of AlGaN is shown with local dose densities of alpha particle collisions. This corresponds to local dose distributions as the number emitted particle approaches 1 billion.

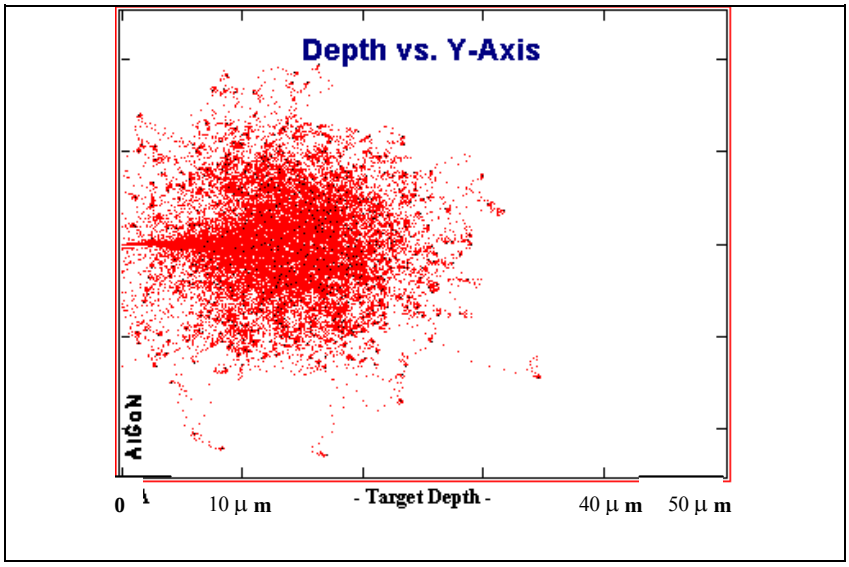

Figure 1.1. Ac-277 Radioisotope Source Penetration in AlGaN. The beam of fresh alpha particles (originating from a point mass of Ac-277) is collimated trough a narrow tube to the left of the 0 point of Figure 1.1.

In Figure 1.2, the graphic result of simulating the dose to the alpha particles from a slab of Ac-227 is given. We see fairly good agreement of between the range of dose in Figure 1.2 and the range of radiation predicted in Table 1.2. Remember that the week beta particles have a slightly (not > 50% more) longer range than the α's from Ac-227.

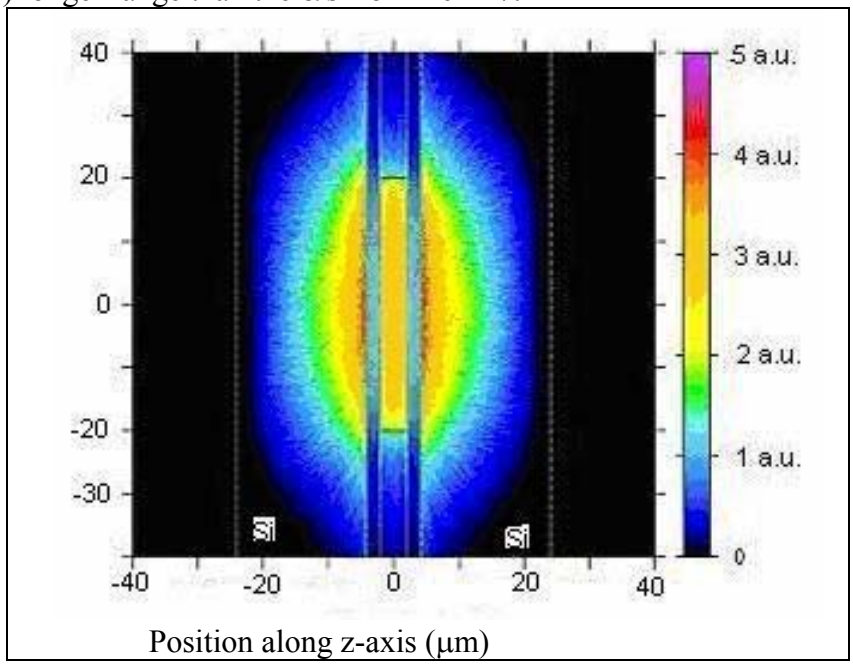

Figure 1.2. Dose distribution to slabs of Silicon due to a radiative source of Ac-227. The fuel source has a width of 0.0003 cm (or 3μm) along the z-axis and has a solid yellow coloring. In length, it extends from -20μm to 20μm along the x-axis.

For every ten CentiGrays of dose in the bulk region imparted by the alpha particles to the Si material, roughly five CentiGrays of dose in the same region is imparted by the more frequent but low energy beta particles. Due to the compatible ranges of the β's and α's from As-277, the dose

contributions from β and α add together fairly evenly between 5 and 12 μmeters from the Ac-227 source. The main simulation of dose distribution for Figure 1.2 was done via MCNPX.

Next we review graphically the dose profile imparted to a slab of AlGaN due to a point source of Ni-63. In scenario of this graph, self absorption due to Ni-63 has been made negligible - since the fuel has virtually zero thickness. Note that the average kinetic energy of a beta particle emitted from Ni-63 is 17.4 keV.

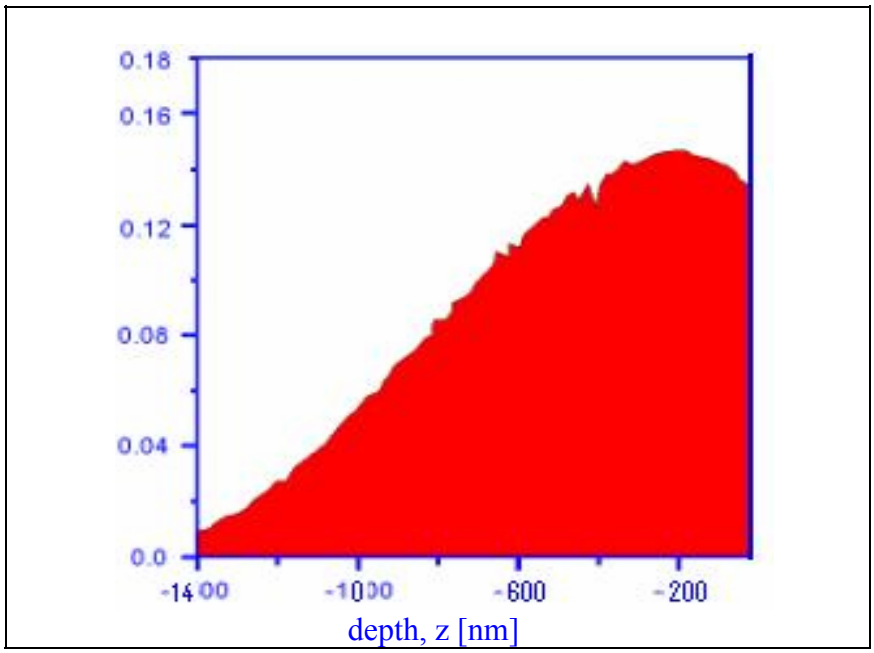

Figure 1.3. Electron energy deposition with depth for AlGaN slab #AGNvzNi mono-energetically averaged point source set at <E> of Ni-63.

The systematic simulations of for Figure 1.3 were done via EGSnrc, which generates dose calculation from electrons more effectively than MCNP. Note that the range of the ensemble of beta particles appears to be roughly -1600 nanometers (negative). If we include the full spectrum of betas from Ni-63 rather than just monoenergetic electrons, the range displayed in the Figure will be larger by more than a factor of three, in keeping with Table 1.2. This would add a modest tail within Figure 1.3.

Discussion of energy imparted to a substrate of semiconductor (to make transducer) from Ni-63 fuel sources shall be continued in Figures 1.8 and 1.9.

Let us return to the consideration of 'fluorescing' component (i.e. C2) of the (M2) type of nuclear battery. It was mentioned that experimental investigation has been done on the performance of Cu+-doped fused quartz glass as a fluorescer or in possible terminology as a phosphorescer. Figure 1.4 is an example of the result of systematic irradiation in lab of Cu+-doped fused quartz.

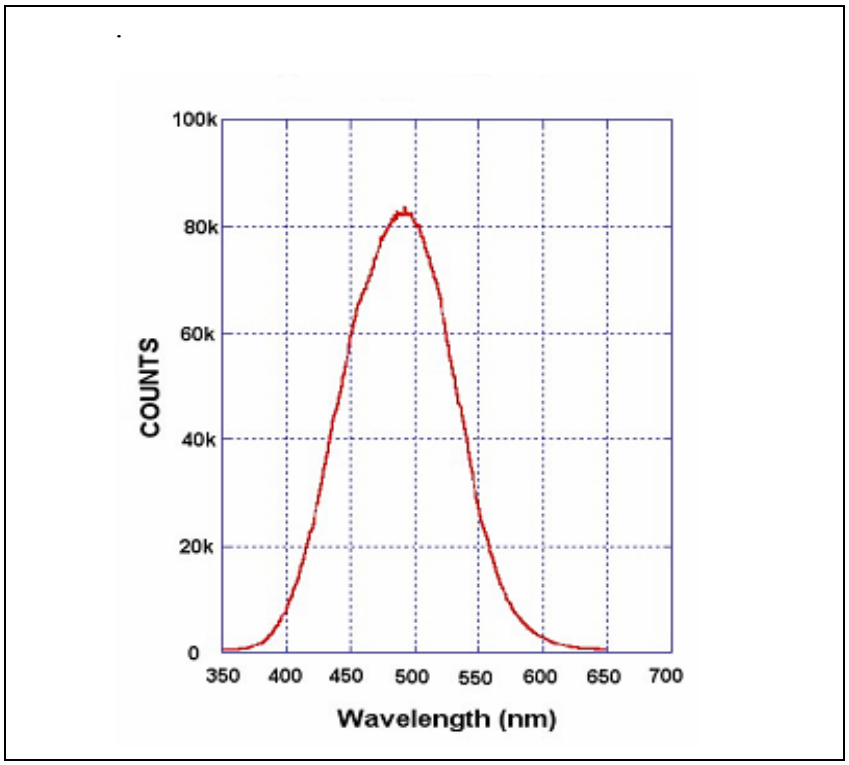

Figure 1.4. Fluorescence Spectra of Copper-Doped Fused Quartz

Useful energetic down-conversion occurs when beta particles or secondary electrons from hard photons (or X- or γ- ray) inelastically collide with the atoms in the medium of Cu+-doped fused quartz glass. Due to principles of radiation dosimetry which also happens to include the premise that much of the dose to material come from secondary electrons, the irradiation of the sample of Cu+-doped quartz would give us similar results or results with even a stronger spectral pattern. Clearly, a non-negligible percentage of the atoms in the metal doped glass respond to the inelastic collision by emitting optical photons in the green energy range.

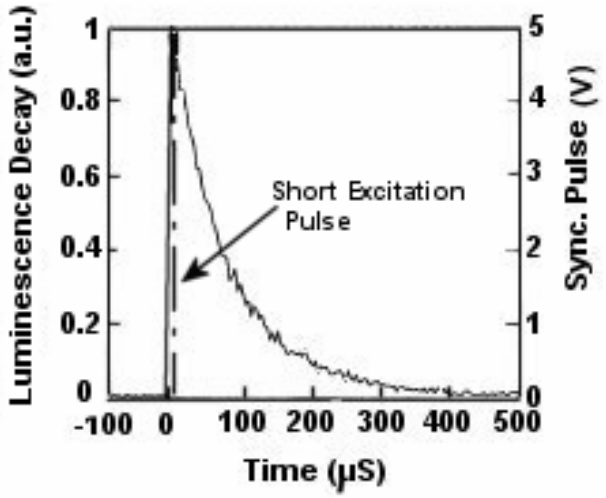

Figure 1.5. Phosphorescence Spectra of Copper-Doped Fused Quartz

The graph of Figure 1.5 is based on illustrative data found in publication [1] supported by the Naval Research Lab. Within this report, we categorize any material which phosphoresces within 1 hundredth of a second of ionizing radiative exposure as being fluorescent. Therefore, the phenomenon shown in Figure 1.4 may be referred to fluorescence in this report. The result shown in Figure 1.5 supports the response sub-millisecond luminescence activation function shown in Figure 1.4. Figure 1.5 demonstrates the luminescent response of the Cu doped fused quartz to pulses of radiative power.

It is also possible to achieve fluorescing of doped glass at rather specific wavelengths of light, but the magnitude of response is weaker than for fused quartz/glass. A very promising phenomenon is that although the structural integrity of quartz declines significantly as a function of dose, the ability of the doped quartz to fluoresce hardly declines at all after extended multi-monthly radiation exposure.

In the remainder of this page, illustrations and descriptions are given of some of the work done in the past year, including FY06/07 and also FY05/06 since the work in FY06/07 on the semiconductor technology has continued from FY05/06.

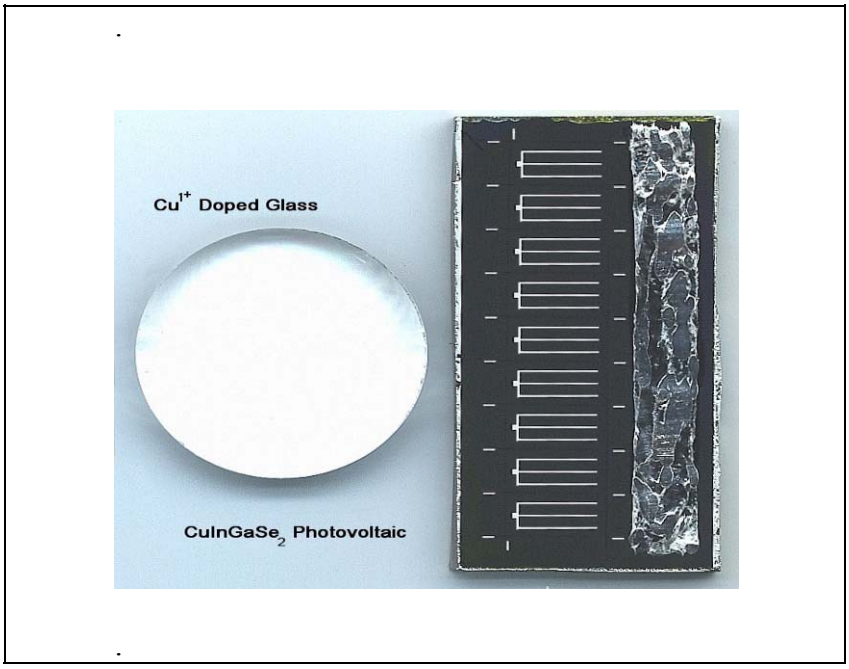

Figure 1.6. Test of Fundamental Radionuclide Conversion with Cu+- Ion Doped Quartz Glass and CuInGaSe2 Photovoltaics. This test was conducted in order to evaluate the concepts of (C2) and briefly (C3) of the (M2) tertiary energy conversion devices, which includes luminescence for the intermediate conversion stage.

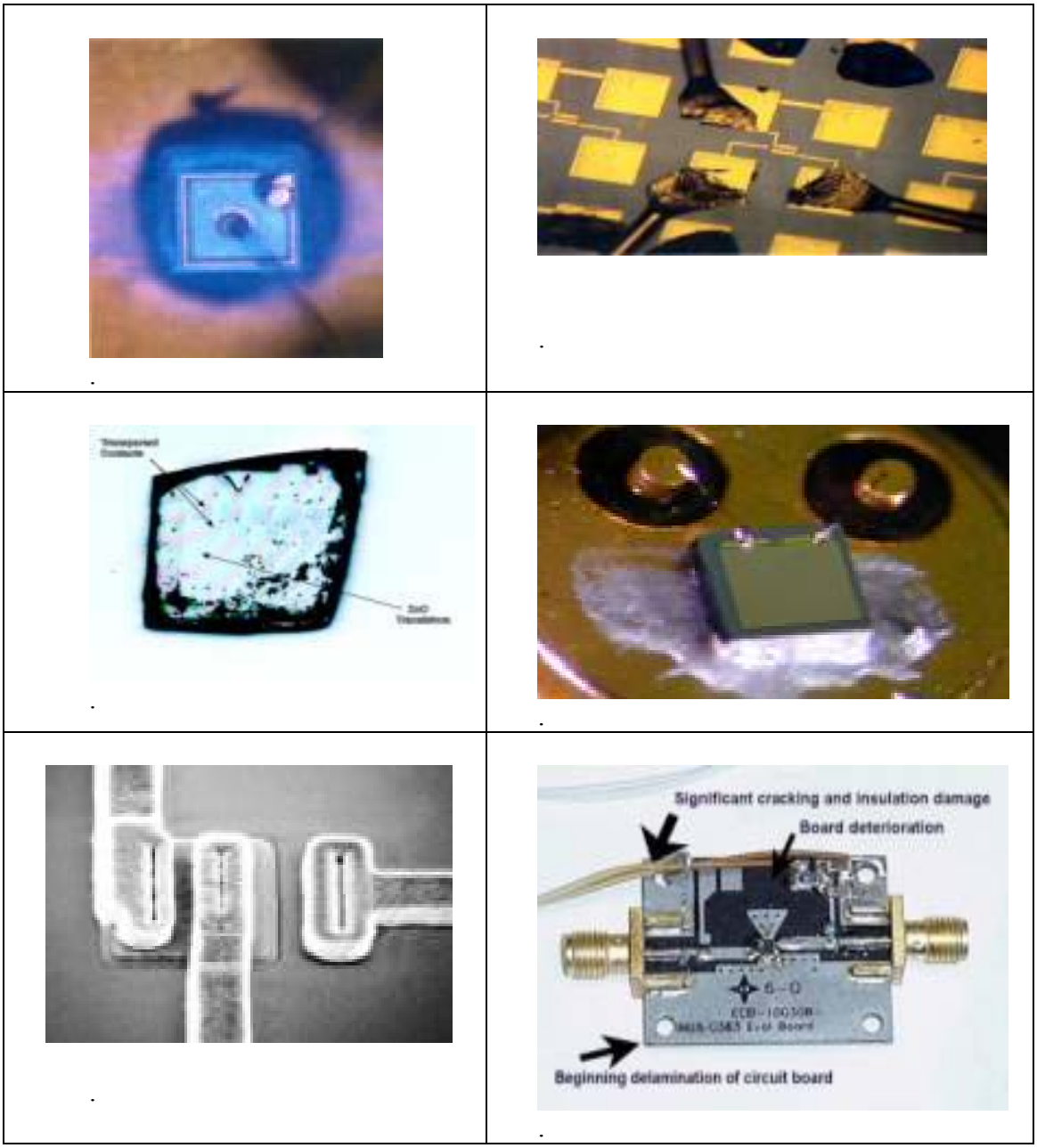

Figure 1.7. Examples of Devices Irradiated: (from top clockwise) GaN, InP, AlGaAs, SiGe, SiC & ZnO. These device samples were tested to evaluate radiation tolerance and damage thresholds in semiconductors.

Briefly let us go back to performances of (C1) the fuel of any betavoltaic cell or nuclear battery of type (M1). Although Silicon based transducers still have challenges in terms of duration of electricity converting performance, such transducers do perform reasonably well in the beginning of lab trials. Let us consider a sandwich of two long slabs of Si which surround one slab of pure Ni-63 fuel which is of variable width X. In Figures 1.8 and 1.9, the number of energetic electrons absorbed by the Si slabs and the power imparted to the Si slabs as a function of X are studied. The slab of fuel is slightly shorted perpendicularly to X-axis than the two Si slabs. One would address the issue of self absorption of beta particles by the Ni-63 fuel.

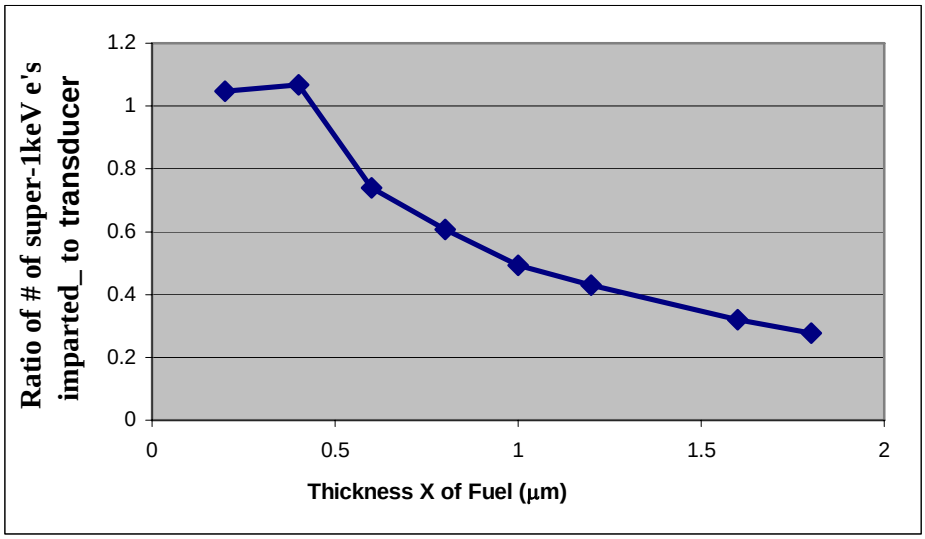

Figure 1.8. Graph of ratio of population of super-1 keV electrons imparted to the transducer substrate (of Si) over the population of beta particles generated in the radioisotopic source versus thickness of the slab of Ni-63. The super-1 keV electrons consist of primary beta particles as well as secondary electrons which are energized electrons liberated by colliding beta particles or other secondary electrons. This figure and Figure 1.9 include the modeling results which are centered by the typically energy beta particle, which is at 17.4 keV (i.e. <E>).

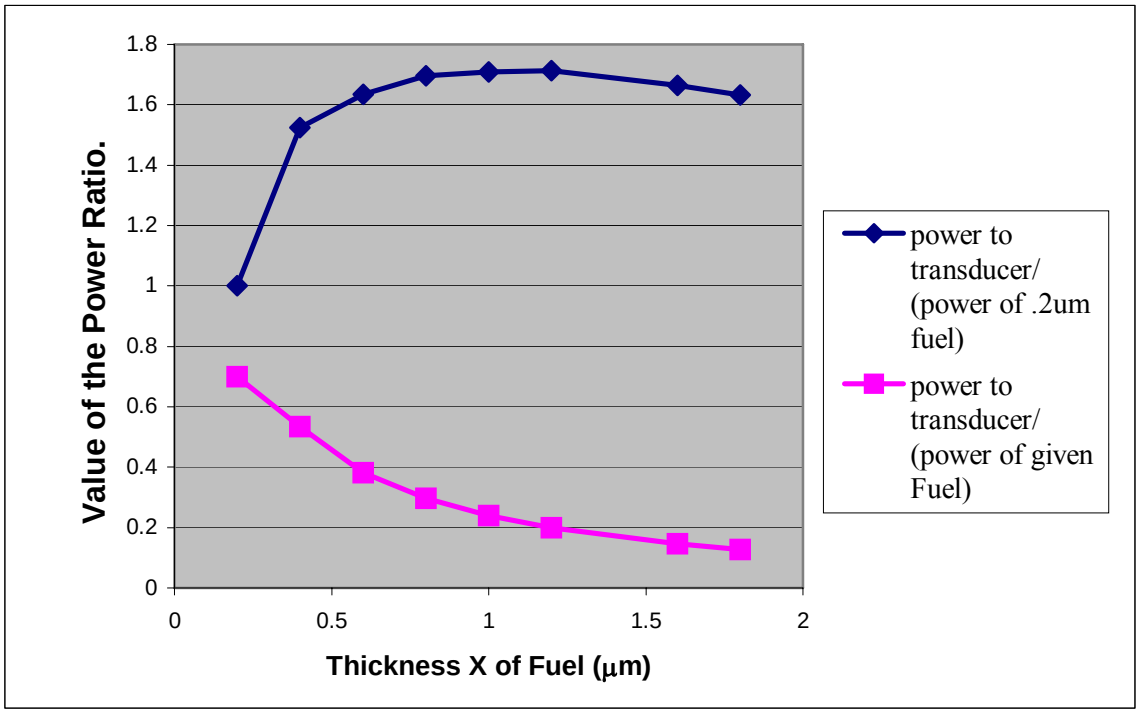

Figure 1.9. Graph of the Ratios of Power Imparted to the transducer substrate (of Si) over the raw power generated by particular choices of thickness of Ni-63 fuel. Figure 1.9 depicts Power imparted to the Si substrate over raw power from fuel with thickness X. The upper graph depicts the ratio of Power imparted (to Si) from fuel with thickness X over Power imparted from fuel with thickness of .2μm.

As is obvious from basic transport theory the ratio of power imparted to Si transducer over raw radiative power approaches on as thickness approaches 0μm. However, in a manner analogous to exponential attenuation, the maximum power imparted by a slab of pure Ni-63 (which should always have r = to 8.88 gm/cc) occurs when the thickness X of slab is 1.1 μm. In terms of use of only a single conversion process, the efficiency at 1.1 mm for X cannot be more than 24% since 76% of power ends up going back to heating up the slab of Ni-63.

1.4 Subsequent Objective

The overall goal is to develop a nano-scale radioisotope powered battery (i.e. a nuclear battery) to provide a durable and uninterrupted power source for MEMS devices and microscopic (and/or submicroscopic) circuit boards for enduring operation through multiple decades. This objective is to be carried out through the development of nano-scale nuclear battery models, designs of such devices, supporting radiation testing of components, and testing of functionality of components. The subsequent objective is to build and test such a submicroscopic nuclear battery. Our group is pursuing development of nuclear batteries of type (M1) and type (M2), which were described in the beginning of Dessign of Nuclear Batteries for Micro and Nano-Scale.

An innovatively small radioisotopic power generator at the nano-scale will have numerous applications of importance. There also are military and security applications of MEMS devices powered by nuclear nano-batteries. Making logical assumptions, you need not know top secret information about warheads to speculate on how and what functions a MEMS nuclear power supply device might contribute to the apparatus. Consider the range of following applications:

1 Independent trickle battery charger for key batteries aboard the RRW device,
2 Powering MEMS on/off switches,
3 Supplying small electrical charges to various components,
4 Warning lights to advise of system leakage,
5 Power supply to in-house corrosion detector – via locally active attraction of ions,
6 Power supplies can run MEMS logic circuitry,
7 Power to run a micro controller, and
8 Warning lights to monitor system integrity.

1.5 Future Work:

In great regard to development to type (M2), fluorescing nuclear batteries, progress has been made the development of copper+-doped quartz as a fluorescing material (generating photons in the visible spectrum →green) which responds to x-rays and beta particles. This is seen through the experimental data of and work behind the data of Figure 1.4. The prior knowledge from Figure 1.5 also is helpful. Further in lab investigation will be made of Cu+-doped fused quartz/glass and of quartz/glass doped with other metals such as Manganese. Doped glass will also be investigated to some extent due to its radiationally desirable amorphous nature.

In terms of forecast for design of a (M2) type of battery, it is already realistic propose the following robust scheme:

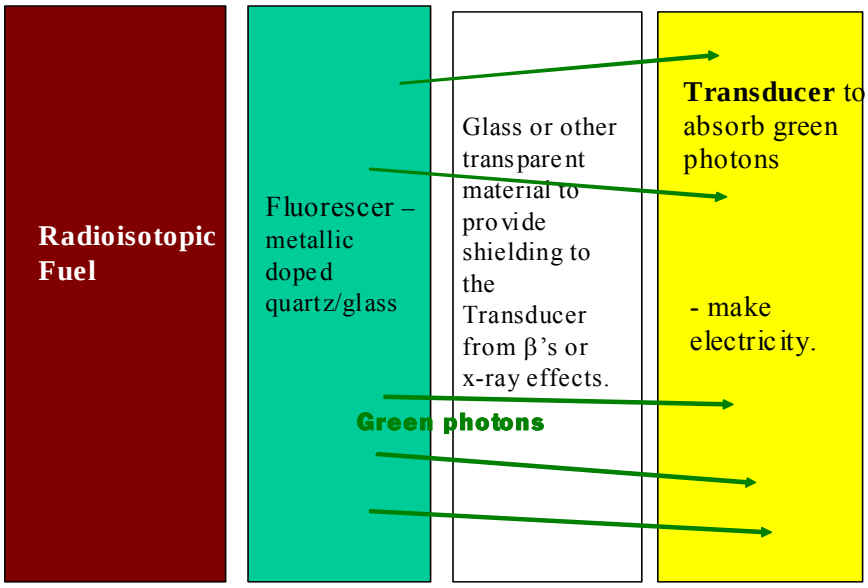

Figure 1.10. A Radiation Hardenable Scheme for the Design of Nuclear Batteries of Type (M2) where a solid fluorescing material such as Cu+-dope quartz is the indispensable link between the fuel and the transducer. The transducer is to be designed to absorb green or yellow light. With enough shielding to lower energy betas SiC could serve as this transducer. This need of the glass shielding in Figure 1.10 allows the use of Ni-63 or a tritium composite for fuel.

In the review of Tables 1.1 and 1.2 within the section of "Discussion of Choices of Radioisotopes." It becomes apparent that three radioisotopes stand out as the most viable candidates for a small nuclear battery to power MEMS devices. These three viable radioisotopes are: Ni-63, and Sm-151, and tritium. It was discussed in that section that penetration distances of the charged particles from the fuel should be a small as possible. Moreover, it was discussed that emitted γ-rays and x-rays should be as low and as infrequent as possible, with energies below 30 keV. Out of these three choices, H-3 and Ni-63 are the best choices. Tritium and Ni-63 do not emit γ-rays. Ni-63 emits bremstrahlung generated x-rays of energy around 10 keV and at lower energies less than 0.3 percent of the time. Sm-151, somewhat unfortunately, does emit an occasional γ-ray at 21.5 keV. Moreover, Ni-63 has a power to fuel mass ratio of $7.5 \cdot 10^{-3}$ Watt/gm rather than lower ratio of $4.0 \cdot 10^{-3}$ Watt/gm of Sm-151. This almost 2-fold advantage of power from Ni-63 combined with the lower incidence of semi hard photons makes Ni-63 more desirable as a radioisotopic fuel source.

If one does not consider the phase of matter nor quality of material, then tritium would turn out to be the best candidate out of our 3 finalists of isotopes. It emits virtually *zero* superkilo-eV photons. And has a grand power to fuel mass ratio of 0.176 Watt/gm. The unfortunate attribute of tritium is that it naturally forms the gas molecule T_2. Moreover, the lowly molar number of 6 of T_2 lends itself to extremely low density at STP of approximately a mere 10^{-4}gm/cm^3. In order to develop a feasible nuclear battery which is fueled by tritium at the nano-scale or even the micro-scale, it will be necessary to develop methods of compressed storage of tritium. One method is that of extreme compression of the tritium into microscopic containers or containers at the millimeter scale. Another method is to develop molecules such as radioactive cetane ($C_{16}T_{34}$) or radioactive octane (C_8T_{18}). These molecules have liquid densities slightly greater than 1 gm/cm^3. The percentage of mass due to the tritium rather than carbon is over 33 percent. Storage of tritium in

such molecules is one way to increase the density of tritium based materials to an order of magnitude comparable to that of water. Another method to consider exploring is the storage of tritium molecules in carbon nanotubes. The nanotube assemblies would have to be made compact in order to achieve reasonable desirable densities such as 0.2 gm/cm^3.

1.6 References

1. M. Plazas, B. Justus, P. Falkenstein, A. Huston, H. Ning, R. Miller; *"Optical Fiber Detectors as in-vivo Dosimetry Method of Quality Assurance in Radiation Therapy,"* Revista Colombiana De Fisica, Vol.37, No.1, 2005.

2. E. Steinfelds, M. Prelas, et al.; *"A Comparison of the Performance Capabilities of Radioisotope Energy Conversion Systems, Betavoltaic cells, and other Nuclear Batteries,"* Proceedings of ICAPP '06; ANS Paper 6408; Reno, NV, June 2006 .

3. M. Chandrashekhar, et al. et A. Lal; "*Demonstration of a 4H SiC Betavoltaic Cell,"* Material Science Forum, Vols. 527-529 (2006), pp. 1351-1354; Trans Tech Publications, Switzerland, 2006.

4. Alan Huston, Brian Justus; *"Optically transparent, optically stimulable glass composites for radiation dosimetry,"* United States Patent 5811822; Assignee: The United States of America as represented by the Secretary of the Navy; Sept. 1998.

2.0 Development of Techniques for 3-D Imaging and Visualization of MEMS

2.1 Purpose and Applications

The National Nuclear Security Administration (NNSA) relies on employing high technology devices and components to execute its mission and ensure national security. There is a clear emphasis toward the miniaturization of many of these devices, with an emphasis on the development on Micro-Electro-Mechanical Systems (MEMS). As the scale of fabrication of MEMS devices decreases, the level of sophistication of device architecture and operations continues to increase. MEMS devices are evolving to complex 3-D structures with increasingly demanding fabrication and assembly requirements. The small size and reproducibility required during assembly has progressed to the point where robotic controlled processes are necessary and the long-term durability of MEMS in critical components remains to be evaluated. Non-invasive inspection and characterization of 3-D visualization in support of these areas is being investigated in order to provide an increasingly quantitative basis for quality assurance, image guided robotics assembly and tools for the characterization of operational tolerances and wear of these devices. The visualization task originally addressed the evaluation of 3-D imaging techniques for quality assurance applications. Specific consideration of utilizing micro-CT was investigated because it offers 3-D imaging capabilities without the deleterious effects of electron beams used for SEM, the tradition technique of choice for imaging MEMS devices.

This task is directed toward the development of techniques for 3-D imaging and visualization of MEMS for the following purposes and applications:

1. Non-destructive evaluation of MEMS devices and components for quality assurance including the evaluation of:

- Production quality and tolerances,
- Durability and wear as related to component design, and
- Component tolerances throughout their service life.

2. Visualization for MEMS assembly with a focus on robotic guidance for positioning and component assembly.

The tasks focus on those applications where 3-D imaging techniques are required by the complex morphologies of individual devices, or limited optical inspection by intervening structural components upon assembly. X-ray imaging techniques have, and continue to be, extended to examine very small scale objects. This work investigates the extension of these techniques to these particular applications.

2.2 Micro-CT Applications

In the previous years simulations were performed in order to determine the optimal materials, beam energies, reconstruction filter, and interpolation method the simulations were run using a sample MEMS device. The results demonstrated the feasibility of performing micro-CT on MEMS components. Subsequently MEMS components fabricated using the LIGA techniques and the Sandia National Laboratory (SNL) were empirically examined using micro-CT. In this year the raw data from these scans was run through a variety of computational simulations to verify the best choice of filter and interpolation method when reconstructing micro-CT images. The results of the simulations based on the empirically collected micro-CT data correlates well with the previously performed simulations based on modeled data.

2.3. Reconstruction Algorithms applied to Empirical Data

The raw sinogram data from Scanco was imported into Matlab in order to verify the previous simulations regarding optimal reconstruction methods. In these tests, the raw data was reconstructed using the previously tested filters and interpolation methods. The contrast-to-noise ratio was calculated for each filter and interpolation method using the procedure previously described for the initial simulations. The values of the contrast-to-noise ratios were then compared to verify the previous simulations with empirically collected data. The results of these tests are shown in Figures 2.1 through 2.4.

As shown in Figures 2.1 and 2.2, the Ram-Lak and Shepp-Logan reconstruction filters provided the best contrast-to-noise ratio, while the simulation predicted that Shepp-Logan and LP cosine filters would produce the highest CNR. Although the results based on the simulated and empirical data sets vary slightly, the general trend of the filter performance remained the same. The CNR values for all experimental results were improved as compared to the initial simulations.

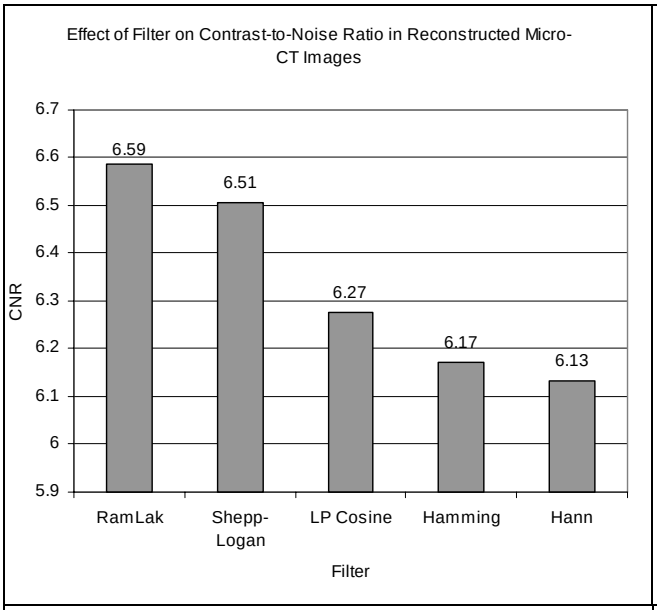

Figure 2.1. CNR for various reconstruction filters based on a simulated MEMS device.

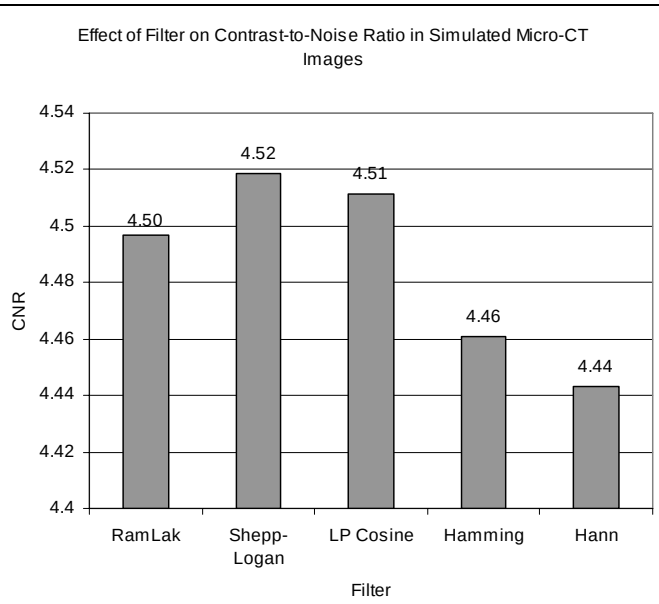

Figure 2.2. CNR for various reconstruction filters based on a micro-CT data of a MEMS component.

Figures 2.3 and 2.4 verify the initial simulations' predictions that the spline filter provides the best image contrast ratio. It should also be noted that, as with the results of the reconstruction filter, all CNR values were higher for the simulations using the experimental scan data as compared to the initial simulations. The slight discrepancies in both the filter and interpolation method data are most likely attributable to the smaller x-ray focal spot size used in the Scanco scanner as compared to the arbitrary size utilized in the initial Matlab simulation. Other contributing factors could include slight differences in experimental setup and scanner geometry between the simulations and the Scanco system.

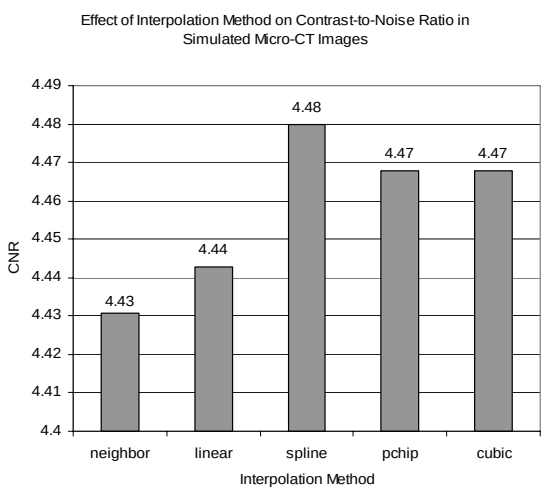

Figure 2.3. CNR for various reconstruction interpolation schemes based on a simulated MEMS device.

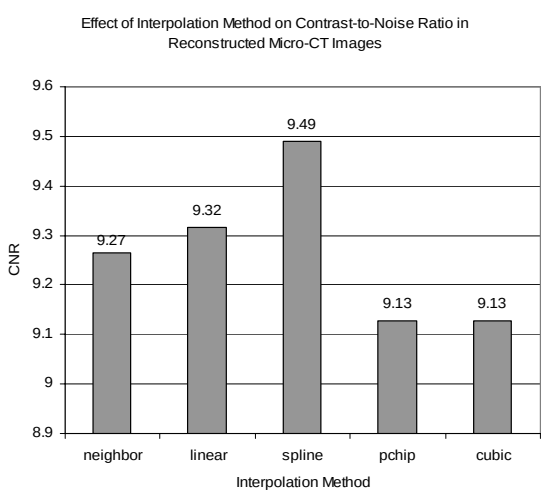

Figure 2.4. CNR for various reconstruction interpolation schemes based on a micro-CT data of a MEMS component.

The results of micro-CT imaging with MEMS components of various architectures show promise for utilizing this method of imaging for nondestructive quality assurance of such devices. Overall component structure is readily visible in 3D-rendered reconstructions taken at a 12 micron resolution, with finer details visible in higher resolution scans. Traditional 2-D presentations readily permit quantitative evaluation of the presented spatial dimensions, but 3-D renderings can enhance the visualization of component morphology and topography simulations and experimental micro-CT images. Both Shepp-Logan and RamLak filters were shown to provide maximal CNR in reconstructed images, and overall contrast levels from experimental scans were found to be much higher than anticipated from original simulations for all filters. The fact that actual scanner performance exceeded that predicted by computer simulations further demonstrates the feasibility of extending micro-CT visualization techniques to more complex MEMS devices.

2.4 Micro-Tomosynthesis (DmTS) Applications

Currently we have performed a thorough investigation of micro-CT performance as applied to the 3-D visualization of MEMS and have optimized a number of micro-CT capabilities, while also identifying micro-CT limitations as applied to our overall goals (NDE of MEMS components and Visualization for MEMS assembly).

Micro-CT has been demonstrated to be a useful tool for the NDE of MEMS components, with continually improving limits on spatial resolution, currently down to about 300 nm (perhaps it will soon be referred to as nano-CT). We have, however, identified issues that limit the applicability of micro-CT, particularly for applications involving “in-service” inspection of MEMS and the visualization for robotics guided assembly. These problems arise due to limited physical access to the device, and long times required for image acquisition and reconstruction, when imaging objects via micro-CT.

Some specific limitations include:

- Small sample space (high resolution micro-CT require samples smaller than about 11 mm diameter).
- Long acquisition times (15-90 minutes)

- Severely limited physical access since the sample object rotates within the x-ray source/detector geometry.

These limitations likely make it necessary to remove MEMS components from service, and also that some components are significantly disassembled in order to perform NDE inspection. In addition the image acquisition, visualization and feedback, are likely to be too slow and cumbersome for effective robotics assembly of MEMS devices.

In order to overcome these limitations we are developing a novel, alternative imaging approach. This extension of digital tomosynthesis to microscopic imaging has not, to our knowledge, been performed using readily available radiation sources. A research group at the European Synchrotron Radiation Facility (ESRF) has demonstrated the technological potential of this technique using monochromatic and white synchrotron radiation. We have performed a feasibility study that indicates that DmTS performed with a micro-focus x-ray source (20 micron focal spot) and a digital flat panel imager of currently available technology should permit the 3-D acquisition with image slices of 10 micron. While DmTS generally sacrifices low-contrast image quality compared to micro-CT, the information content of the image is equivalent over a limited angular range. The fewer angular projections required for DmTS (compared to micro-CT) permits both more rapid image acquisition and more rapid image reconstruction. Perhaps most importantly, the open geometry of the system better accommodates robotic manipulators for device assembly.

A brief list of advantages of DmTS over micro-CT includes:

- Open geometry accommodates robotic guided MEMS assembly,
- Faster data acquisition,
- Faster reconstruction,
- A-priori knowledge of objects can be integrated to accelerate reconstruction and eliminate artifacts, and
- Rapid acquisition and reconstruction provide faster feedback for robotic guided assembly.

Specific accomplishments and the status of our investigations of DmTS currently includes:

- Evaluated feasibility and reasonably achievable resolutions limits for DmTS (3-D imaging to 10 μm),
- Constructed DmTS simulator for simulating image acquisition and reconstruction parameters, and
- Demonstrated reconstruction and successful filtered reconstruction algorithm.

The DmTS simulator has served as a test-bed for demonstrating the feasibility and exploring optimization parameters for MEMS applications. Figure 2.5 illustrates some early results of DmTS simulation on a simple 3-D monolithic structure. This figure shows a simulated 3-D monolithic structure with a cuboidal void located at the center of the object. A simulation is subsequently performed of the object and the raw data is can be rapidly reconstructed for any desired axial slice within the object. A simple unfiltered reconstruction is illustrated as the second step in the figure. This step reproduces the major structural information but contains significant blurring. The blurring is readily removed by a final filter to produce a clear representation of the central axial slice of the object. The integration of filters into the reconstruction algorithm using DmTS results in minimal additional computational time and can therefore help to provide real-time 3-D imaging feedback for robotically guided assembly of MEMS.

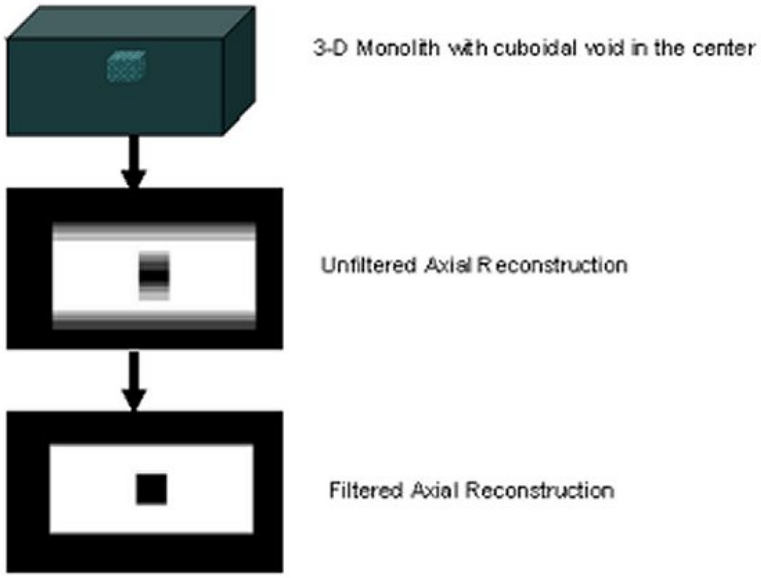

Figure 2.5. Illustration of 3-D DmTS simulation process. This figure demonstrates the ability to obtain axial style images of the target structure as well as the effectiveness of a simple and fast reconstruction filter to optimize the image's information content.

3-D visualization of MEMS components provides a powerful tool for the successful incorporation of MEMS into wide variety of NNSA applications. The project provides the means to quantitatively inspect the tolerances and specifications of MEMS both as they are produced and throughout their service life in the field. DmTS offers the potential for inspecting and characterizing MEMS components with minimal disassembly of larger components, expediting their evaluation and return to service. The 3-D visualization methodologies being developed also support the robotically controlled assembly of MEMS. DmTS provides a feasible technique for providing essential feedback to the guidance and control system for robotics guidance.

2.5 References

[1]American Association of Physicists in Medicine, AAPM Report No. 1, *"Phantoms for Performance Evaluation and Quality Assurance of CT Scanners"* AAPM, Chicago, Illinois, 1977.

[2]American Association of Physicists in Medicine, AAPM Report No. 39, *"Specification and Acceptance Testing of Computer Tomography Scanners"* AAPM, New York, NY, 1993.

[3]J. T. Bushberg, J. A. Seibert, E. M. Leidholdt, J. M. Boone, "*The Essential Physics of Medical Imaging,"*Lippincott Williams & Wilkins, Philadelphia, PA, 2002.

[4]P. C. Johns, M. Yaffe, *"Scattered Radiation for Fan Beams,"* Med. Phys., 9:231-239, 1982.

[5]R.F. Fisher and D.E. Hintenlang, *"Micro-CT imaging of MEMS components,"* Journal of Non-Destructive Test, Submitted for publication, 2007.

3.0 Level II: Research in Macro and Micro Force Control Technologies

3.1 Objective

This research area is concerned with the control of contact forces at the micro and macro scale during in-contact robotic operations. At the micro scale, University of Florida researchers are investigating how force control technologies that incorporate tensegrity principles can be applied to the problem of micro-assembly. This includes design and modeling of a spatial micro-scale force control mechanism. At the macro-scale, the objective of this research is to develop passive and active mechanisms that incorporate compliance in order to control contact forces during manipulation tasks.

3.2 Description of Work Accomplished

3.2.1 Level III: Compliant Spatial Micro-Mechanisms

Mechanisms formed by rigid links and rigid joints have been the object of extensive studies for the theory of mechanisms. These kind of devices are well suited to work at the macro-world, however when the dimensions of the systems are on the order of microns, limitations due to manufacturing processes impose severe limitations, and the generation of motion requires alternative approaches.

Devices for micro-electro-mechanical systems (MEMS) are basically planar devices. This is due the current manufacturing techniques that are derived from the integrated circuit industry. Creating 3D structures at the micro level is a difficult task. Most of the motion of MEMS devices is constrained to the plane. Some works have been made to create spatial motion.

3.2.2 Out-of-Plane Motion Devices

Out-of -plane actuators can convert input signals into displacements normal to the surface of a substrate. Three-dimensional micro-devices are useful for different tasks as for example, object positioning, micromanipulators, optical scanners, tomographic imaging, optical switches, microrelays, adjustable lenses and bio-MEMS applications.

To obtain out-of-plane motion is a challenging problem and several approaches based have been proposed. Usually out-of-plane actuators are multilayer structures, although single layer devices have been reported by Chen [1]. Generally speaking current solutions are based on vertical comb drives, on the deformation of the materials or on the assembly of basic linkages. The following references report out-of-plane motion devices.

Vertical comb drives are formed by an array of capacitors. When a voltage is applied, the movable components of the capacitors rise out of the plane. They are combined with torsion mirrors to tilt micromirrors as it is described by Milanovic [2] and Lee [3]. The vertical motion of comb drives is limited and they require a careful design and control to avoid jumps associated with the pull-in voltage, see Bronson and Wiens [4].

Combination of TiNi and Si cantilever or other substrates such as SU-8 or polyamide have been used to create out-of-plane motion devices. Fu [5] reports several devices based on a TiNi film which is actuated when a current is applied to the electrode.

A micro mirror having a large vertical displacement has been presented by Jain and Xie [6]. The mirror plate is attached to a rigid silicon frame by a set of aluminum/silicon dioxide bimorph beams. A polysilicon resistor is embedded within the silicon dioxide layer to form the heater for thermal bimorph actuation.

Ebefors [7] and Suh [8] implemented conveyors systems for out-of-plane motion able to perform complex manipulations. They are based on arrays of structures that can deflect out of the plane due to different coefficients of thermal expansion. Objects that are placed on the array can be moved according to the deflection of each actuator.

Schwizer [9] reports a monolithic silicon integrated optical micro-scanner. The device consists of a mirror located on the tip of a thermal bimorph actuator beam and it is able to achieve large scan angles.

The other alternative to achieve out-of-plane motion is the assembly of planar linkages. A platform described by Jensen [10] has three degrees of freedom and the top platform remains horizontal throughout the device's motion. A proposal for a three degree of freedom parallel robot is presented by Bamberger [11]. The device uses only rigid revolute joints. Both revolute actuators are located at the base during the manufacturing process, making the device suitable for MEMS fabrication.

Out-of-plane motion has also been realized through the use of elastic elements. A device actuated by comb drives is presented by Tung [12]. Drives are connected to a platform made of polydimethilsiloxane (PDMS) via thin flexural microjoints.

Previous works suggest that compliant links and elastic joints may be a feasible alternative to create mechanical devices at the microlevel. There are many configurations based on these simple elements, one example of which are tensegrity structures and they illustrate another way to obtain spatial motion.

3.2.3 Tensegrity Structures

The word tensegrity is a contraction of tension and integrity and refers to structures formed by rigid and elastic elements that maintain their shape due only to their configuration. Rigid elements do not touch one another and they do not require external forces to maintain their unloaded position (Figure 3.2.2.1).

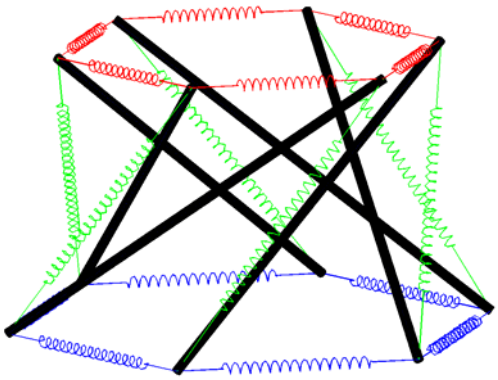

Figure 3.2.1.1. Prismatic tensegrity structure with 6 struts.

Tensegrity structures were developed by architects in the middle of the last century. Research began with Fuller [13]. First contributions were made by Kenner [14] and Calladine [15]. Static and dynamic analysis studies have been made Murkami [16] and Correa [17]. Proposed

applications include antennas, Knight [18], flight simulators, Sultan [19], deployable structures, Tibert [20], and force and torque sensors, Sultan [21]. Tensegrity has been also proposed by Ingber [22], to explain the deformability of cells.

Due to the presence of elastic ties, tensegrity structures are foldable. If in the folded position external constraints are released, they can recover suddenly their original shape by themselves. The deployment can be also achieved in a controlled way using telescopic struts, see Furuya [23] or controlling the elastic ties, see Sultan [24].

Figure 3.2.1.2 shows the same principle but in this case links are not rigid but rather are compliant. When the radius of curvature is changed, the whole structure is able to move in 3D following a complex path.

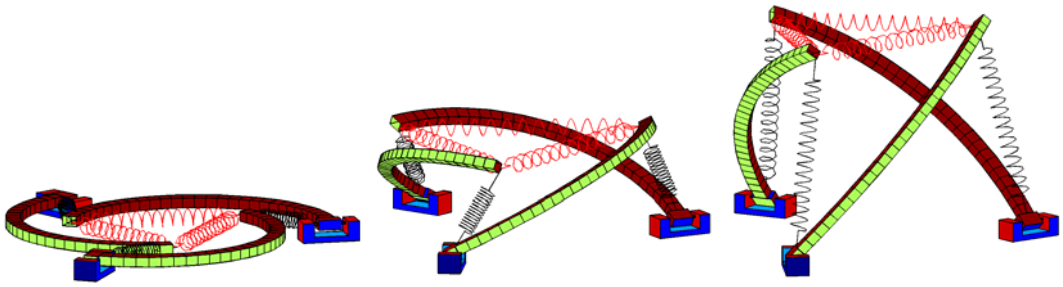

Figure 3.2.1.2. Sequence of motions for the rising of the structure.

Although the device seems feasible, the manufacture of the required joints is very complex at the MEMS level, however it is possible to modify its constitutive elements to reach the same result in a simpler way. Before presenting the idea to be developed in this research it is important to consider in more detail the requirements for the actuators and the joints.

3.2.4 Bimorph Actuators

The bi-layer electrothermal actuator combines two materials with different coefficients of thermal expansion (α). The layers are joined along a common interface and the entire device is heated. Since one material tries to expand more than the other but is restrained by the joint with the second material, the entire structure bends, see Pelesko [25]. It is possible to extend and contract the beam by controlling the temperature of the beam via the use of a resistor embedded in the beam. The electrothermal actuators have the advantages of low operation voltage, a simple fabrication process, and are CMOS-compatible. Therefore, control circuits can be integrated with the device on the same chip. A bimetallic actuator is illustrated in Figure 3.1.1.3.

Figure 3.2.1.3. Configuration of a bimetallic actuator.

If it is true that $\alpha_1 > \alpha_2$ the structure bends with an increase of temperature as shown in Figure 3.2.1.4A. If it is true that $\alpha_1 < \alpha_2$ the structure bends like in Figure 3.2.1.4B. It is usual that the bending of the beam take place out of the plane, but there is not any restriction to bend the beam in the plane.

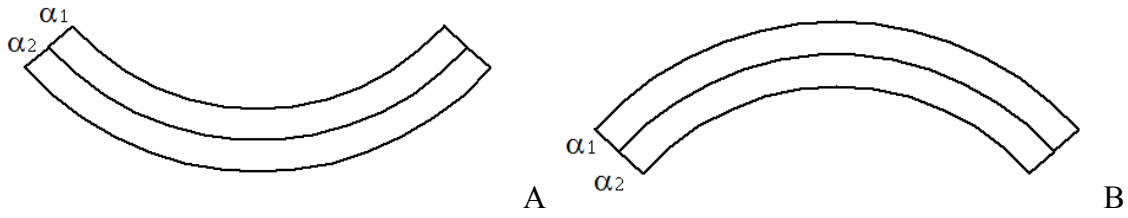

Figure 3.2.1.4. Bending of a bimetallic actuator. A) $\alpha_1 > \alpha_2$. B) $\alpha_1 < \alpha_2$.

3.2.5 Elastic Joints

The functionality of the device is intimately related to the elastic elements located at the ends of the beams. The development of torsion springs at the microlevel has been achieved and presented by Hah [26]. However the development of linear springs is less frequent. Regular-coiled carbon fibers have been obtained by Yang [27], using chemical procedures, also the design of a vertical linear conical microspring attached to the substrate is reported by Hata [28]. None of these ideas are appropriate for a 3D device and for the purpose of this work it is necessary to find an alternative.

The decision about the material and the shape and process must include the following considerations: material with low Young modulus, applicable through spinning and be photo definable, resistant to heat to avoid future complications due to the actuation of the beams, and compatible with the other processes involved in the tensegrity based MEMS device.

3.2.6 The Device

Figure 3.2.1.5 shows a scheme of the device that was addressed in our research. It can be considered as a simplification of the tensegrity system presented in Figure 3.2.1.2. The system maintained its shape due to the upward deflections of the beams. It was formed by three sets of bimorph actuators which transmitted their motion to the central platform through compliant joints. The moving platform could be described by an equilateral triangle. The fixed ends of the actuators were distributed along the vertexes of an equilateral triangle.

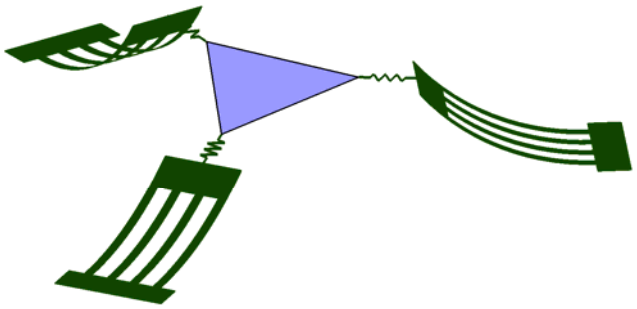

Figure 3.2.1.5. Scheme of the device.

The position of the device is influenced by the stiffness and free lengths of the ties, the location and nature of the joints, and the length and the current curvature of the beams. The presence of elastic elements increases the complexity of the mathematical model that describes the relations between internal forces and the positions of the beams.

3.3 Device Design

Prior to the device design it is necessary to find a mathematical model to describe the kinematics of the system. This issue is addressed in a separate paper. Once the kinematics of the system is understood, the next step is to design the device. This includes the selection of the dimensions and materials for all the elements to obtain a reliable platform.

The critical elements in the device are the actuators and the springs that join the actuators to the moving platform. Their design requires assumptions to simplify the analysis, procedures and analysis techniques from the area of strength of materials, and information from previous experiences for the issues where analytical approaches cannot be implemented.

3.3.1 Actuator Design

Bimorph beams can provide motion out of the plane when they are heated if the difference between the thermal expansion coefficients of the material forming the beams is significant. Also, since the kinematic model assumes that the links are rigid, it is important to limit the deflections at the end of the beams that would result from the forces applied at the end of the beam by the spring element.

3.3.2 Materials

A pair of materials that can be used for the beams are aluminum and silicone dioxide. Table 3.2.1.1 summarizes from Senturia [29], some material properties for the beams. There is an appreciable difference in their coefficients of thermal expansion. In addition these materials are very common in MEMS micro fabrication, therefore there are well established procedures for their deposition and etching processes.

Table 3.2.1.1 Mechanical and thermal properties for aluminum and silicone dioxide.

Material	Young modulus, E MPa	Thermal exp. coeff, α $\frac{1}{K \ 10^{-6}}$
S_iO_2	70000	0.7
Al	69000	23.1

3.3.3 Width of the Beam

For details associated with the manufacturing process, it is convenient to avoid large values for the width of the beam to make it easier to release the beam using isotropic etching. A width of 7 μm is recommended.

3.3.4 Deflection and Length of the Beams

Deflection of the end of the beam is strongly influenced for the length of the beam. For an initial estimation of the deflection it can be assumed that the beams are made of one material. This assumption is justified in the fact that for both aluminum and SiO2, their Young's modulus is almost the same (Table 3.2.1.1). If it is assumed that the beams are straight, from strength of materials the deflection produced by a force at the free end of a cantilever beam, see Boresi [30] and Figure 3.1.2.6, is given by

$$\delta_a = \frac{L_a^3}{3EI} F_a \text{ , where } I = \frac{1}{12} wt^3$$

then

$$\frac{F_a}{\delta_a} = \frac{Ewt^3}{4L_a^3} \qquad (1)$$

where

δ_a : deflection at the free end of the beam

F_a : force applied at the free end of the beam

L_a : length of the beam

E: Young's modulus

w: width of the beam

t: thickness of the beam

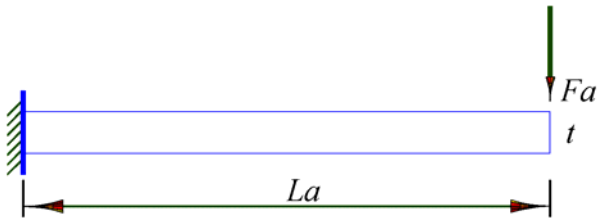

Figure 3.2.1.6. Maximum deflection of a cantilever beam.

Equation 1 can be solved for several length, width and thickness of the actuators (Figure 3.1.2.7). From the point of view of manufacturing, length of the beams is not a constraint, and the larger beams, the higher motion out of the plane, but at the same time to avoid that deflections increase dramatically, the thickness must increase. Large thickness are difficult to obtain therefore they are limited by the manufacturing process. Guided for these reasons the length of the beam is selected as 200 μm and the total thickness (this is aluminum and silicon dioxide) as 3 μm, then from Equation 1 and with w=7 μm

$$\frac{F_a}{\delta_a} = 0.41 \frac{\mu N}{\mu m}$$

The current selection establishes that if the maximum deflection is limited to 1 μm, then the vertical force acting in each beam is $F_a = 0.41$ μN. If each actuator has 12 beams, then the maximum perpendicular force that can be applied to the system is

$$F_p = 12 * F_a \approx 5 \text{ μN} \quad (2)$$

3.3.5 Out-of-Plane Elevation

The design of the spring requires knowing its maximum deflection and one of the factors that influences this parameter is the elevation of the free end of the beam. The maximum deformation of the spring is obtained when the beams reach their maximum height (Figure 3.2.1.8A). This situation occurs at the end of the manufacturing process, when the beams are released from the substrate.

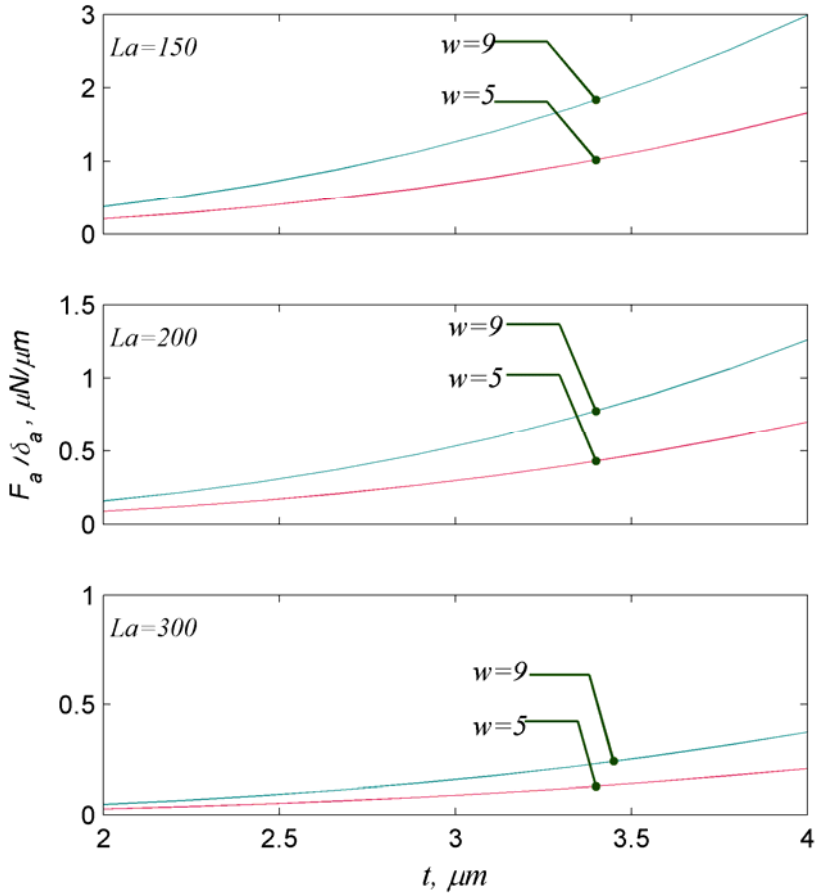

Figure 3.3.1.7. Deflection of the free end for several conditions.

From Figure 3.3.1.8B it is clear that the height of the free end is given by

$$Q_z = \rho(1 - \cos\phi) \quad (3)$$

where

ρ : radius of curvature and ϕ the angle of ρ with the vertical.

From Figure 8B

$$L_a = \rho\phi \quad (4)$$

Substituting Equation 3.2.1.4 into Equation 3 yields

$$Q_z = \frac{L_a}{\phi}(1-\cos\phi) \qquad (5)$$

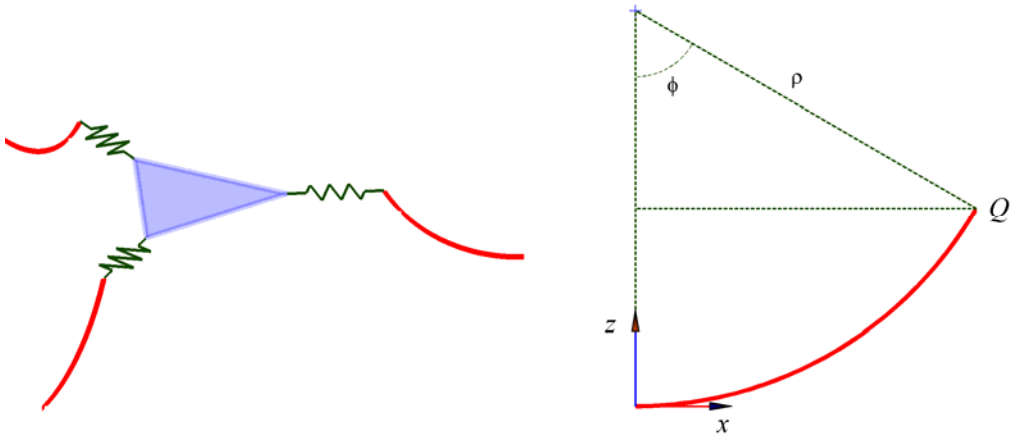

Figure 3.3.1.8. Maximum elevation of the free end of the beam. A) Isometric view. B) Lateral view.

Equation 3.3.1.5 evidences the dependence of Q_z on ϕ, however the value of ϕ is difficult to obtain analytically. At the end of the manufacturing process and before releasing from the substrate, the beams are in the plane but intrinsic stresses are present. They appear because the materials are deposited at a higher temperature and after the etching process the two materials cool to ambient temperature. Once they are released from the substrate, the beam curves up to release the stresses (Figure 3.3.1.9).

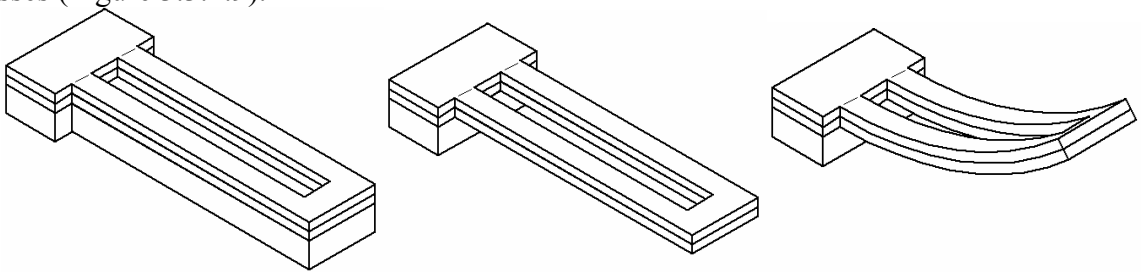

Figure 3.2.1.9. Bending after release from substrate.

The initial value of the radius of curvature ρ and therefore the initial value of angle ϕ depend on the geometry and material properties of the bimorph beam. Liu [31] presents the following equations that should permit the evaluation of the initial radius of curvature of a bimorph beam. When the thickness of the two layers is the same and the Young's modulus is equal the radius of curvature is given by

$$\rho = \frac{8}{3}t\ \frac{E}{\sigma_2(1-\nu_2)-\sigma_1(1-\nu_1)} \qquad (6)$$

where

σ : intrinsic stress in the layers after deposition

ν : Poisson's ratio for the layers

and subindex 1 is for the material at the bottom and subindex 2 is for material on the top.

To be useful for numerical evaluation, Equation 6 requires the knowledge of the intrinsic stresses σ_1 and σ_2. They depend strongly on all the conditions for the manufacturing process and also on the thickness of the layers. For the same reason, very few values are referenced, and in the best of the cases only ranges of values varying from negative to positive can be obtained. In the absence of better information, Equation 6 cannot be applied and the estimation of angle theta must be done from previous experiences. Xie [6] reports that from a beam of similar length an angle ϕ of 17º has been observed. For purposes of this design, angle ϕ is assumed to be 20º. The exact value is not of interest as well as the spring be able to yield the maximum deformation without excessive stress that may damage it.

3.3.6 Springs Design

The spring must be able to provide the maximum deformation required for the mechanism and stand the stresses generated by this deformation. The first step it to evaluate the maximum elongation that the springs must provide.

3.3.7 Springs Elongation

When the device is on the horizontal plane the lengths of the springs correspond to the free length d_0 (Figure 3.3.7.10A). When beams reach the maximum elevation (Figure 10B), the length of the springs is maximum.

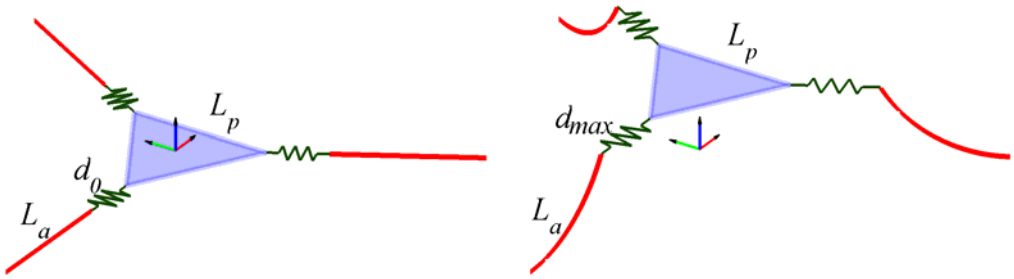

Figure 3.3.7.10. Positions for minimum and maximum deformation of the springs. A) Initial position. B) Maximum deformation position.

The kinematics analysis of the mechanism permits one to evaluate the position of the platform given the points *Q*, and therefore the maximum elongation of the springs, $d_{\max} - d_0$, for several values of the parameters of the device. A set of results is presented in Figure 3.3.7.11 for a length of the actuator $L_a = 200$ µm, free length of the spring $d_0 = 80$ µm, and the length of the side of the platform $L_p = 120$ µm.

Values of d_0 cannot be very small to avoid exaggerated stresses. For the current values of L_a, L_p d_0 and for the already selected value of 20º for ϕ, the maximum deformation is 4.0 µm. This is the elongation that the spring must provide.

3.3.8 Maximum Force Acting on the Spring

Force acting on the spring must be limited. If this force is excessive its vertical components acting on the beams may generate a deflection larger than the design value.

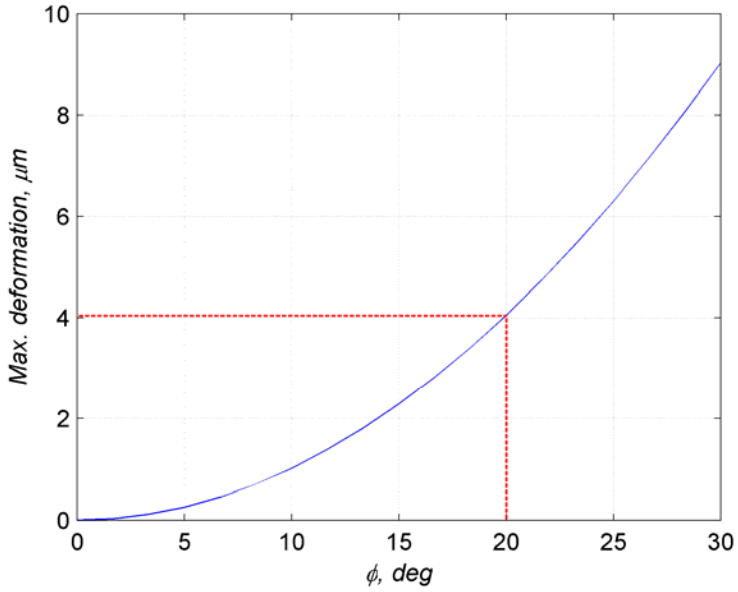

Figure 3.2.1.11. Maximum deformation of the springs.

Figure 3.3.8.12 shows the components of the force acting on the spring. In Equation 2 the maximum admissible perpendicular force was selected as $F_p = 5\,\mu\text{N}$ and then when F_s is maximum

$$F_s = \frac{F_p}{\cos\eta}, \text{ where } \eta = \frac{\pi - \phi}{2} \qquad (7)$$

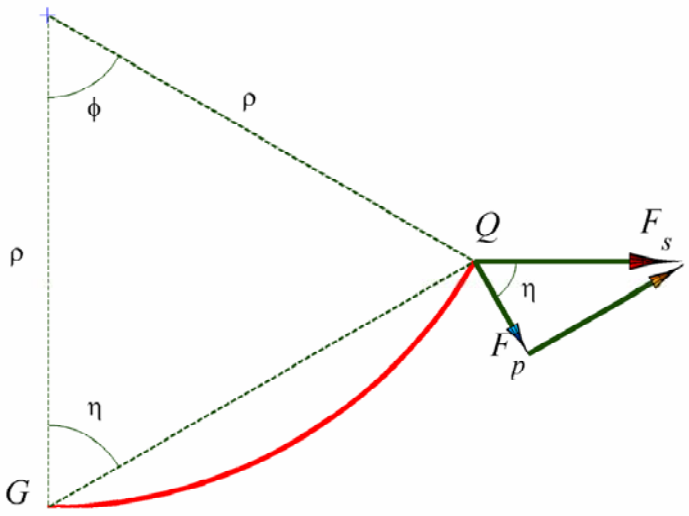

Figure 3.3.8.12. Maximum force in the spring.

For $\phi = 20^\circ$, Equation 7 yields $\eta = 80^\circ$ and $F_s = 28.8$ μN.

In summary, to get a maximum deformation of 4.0 μm the maximum force cannot exceed 28.8 μN, in order to keep the component perpendicular of the force to $\overline{GQ}$ less than 5 μN.

3.3.9 Spring Geometry and Material

The simplest geometry for the spring is a bar with rectangular section, similar to a common tie (Figure 3.3.9.13A). However, to obtain significant deflections with that geometry requires a material like rubber that is able to deform with low external forces. Some tests were performed in the laboratory using different kinds of silicone rubber. However due to the fact that the dimensions of the ties are very small compared with the other components of the device there was no evidence that the silicone filled the channels. Another undesirable aspect with this material is the difficulty to etch it with conventional plasma. Since ties are essential to this work it was necessary to look for other alternatives. A simple one is to change the geometry of the spring. If instead of a simple bar, a shape like the presented in Figure 3.3.9.13B is used, it is easier to achieve the required deformations.

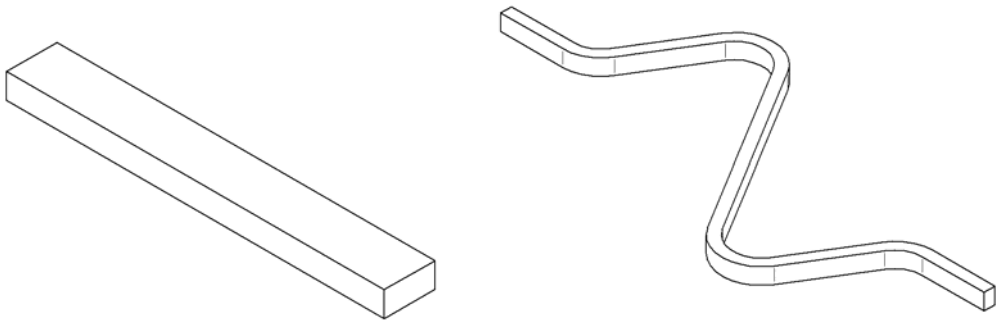

Figure 3.3.9.13. Possible geometries for the spring. A) Bar. B) By segments.

Although it is possible to create the spring using the same materials for the beam, this is aluminum and silicone dioxide, their stiffness is still high. One alternative is to use photo definable polyamides. They have low modulus, and in addition can be patterned easily, which is a very important advantage. Table 3.3.9.2 shows some properties of the polyimide HD-8000 from HD MicroSystems. For the following analysis they are considered as isotropic materials.

Table 3.3.9.2 Properties of polyamide HD-8000.

Viscosity St	Thickness μm	Cure ºC	Tensile MPa	Modulus MPa
3.5	3 to 5	350	122	2500

Figure 3.3.9.14 shows the geometrical parameters for a segment of the spring. If T and H are given, angle λ and length L_C can be evaluated as follows

$$2r\cos\lambda + L_c \sin\lambda = T \quad (8)$$

$$-2r\sin\lambda + L_c \sin\lambda = H \quad (9)$$

Squaring Equations 8 and 9 and adding the results yields

$$4r^2 + L_c{}^2 = T^2 + H^2 \quad \therefore \quad L_c = \sqrt{T^2 + H^2 - 4r^2} \quad (10)$$

Since L_C must be positive, Equation 10 shows that the selection of T and H must fulfill the relation

$$T^2 + H^2 \rangle 4r^2 \qquad (11)$$

If Equation 3.3.9.8 is multiplied by $\sin\lambda$ and Equation 3.3.8.9 is multiplied by $\cos\lambda$ and the results are added yields

$$H\cos\lambda + T\sin\lambda - L_c = 0 \qquad (12)$$

Equation 3.3.9.12 can be solved for λ using the trigonometric method presented by Crane [32].

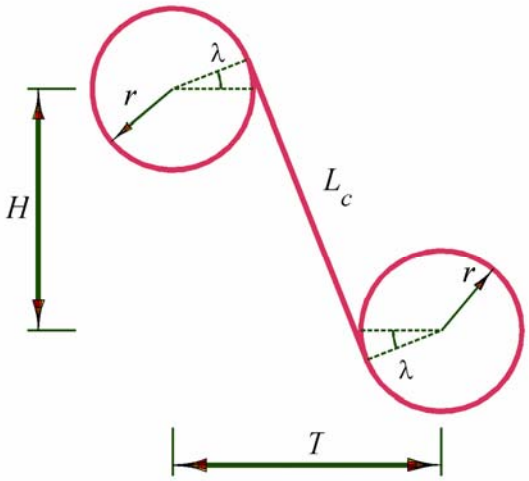

Figure 3.3.9.14. Geometry of a segment of the spring.

3.3.10 Spring Stress

Since the geometry is simple, it is interesting to find analytical relations for the stress and the deflection of one segment of the spring (Figure 3.3.10.15). The maximum tensile stress $\sigma_{\theta\theta}$ occurs at point B (Figure 3.3.10.15).

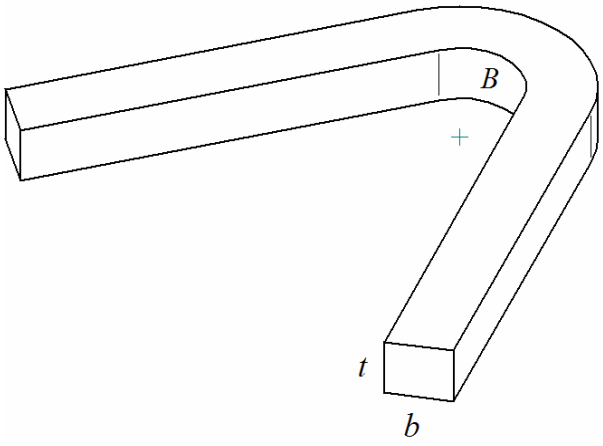

Figure 3.3.10.15. Segment of the spring.

Figure 3.3.10.16 presents the nomenclature to derive the expressions for the circumferential stress in a curved beam following the procedure explained by Boresi [30]

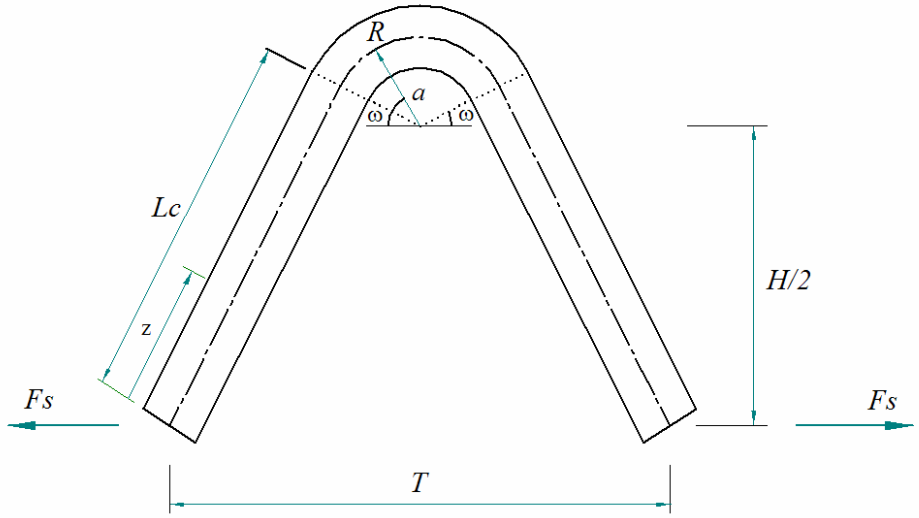

Figure 3.3.10..16. Parameters for the stress analysis of a spring.

$$\sigma_{\theta\theta} = \frac{F_s}{A} + \frac{M_x\left(A - R_i A_m\right)}{A R_i \left(R A_m - A\right)} \tag{13}$$

where

$$A = tb \tag{14}$$

$$M_x = F_s\left(\frac{H}{2} + R\right) \tag{15}$$

$$R_i = R - \frac{b}{2} \tag{16}$$

$$A_m = t \ln \frac{2R + b}{2R - b} \tag{17}$$

3.3.11 Spring Deflection

For the element shown in Figure 3.3.11.15 and 3.3.11.16, the total deflection can be considered as the superposition due to the deflection of the linear segment and the deflection due to the curvilinear segment. Moreover, when the relation *R/b*>2, the effect of shear and normal forces can be neglected. For this case the deflection of the straight element δ_r , is given by

$$\delta_r = 2\int_0^{L_c} \frac{M}{EI}\frac{\partial M}{\partial F_s} d_z \tag{18}$$

where

$$M = F_s z \cos\omega \tag{19}$$

From Equations 3.3.11.18 and 3.3.11.19 and considering a rectangular cross section for the spring (Figure 3.3.11.15)

$$\delta_r = \frac{2F_s L_c^3}{3EI}\cos^2\omega, \quad I = \frac{1}{12}tb^3 \tag{20}$$

The deflection of the curvilinear segment, δ_c is given by

$$\delta_c = \int_w^{\pi-\omega} \frac{M_x}{E}\frac{\partial M_x}{\partial F} Rda \tag{21}$$

where (Figure 16)

$$M_x = F_s\left[L_c\cos\omega - R\sin\omega + R\sin(\omega + a)\right] \tag{22}$$

From Equations 21 and 22

$$\delta_c = \frac{PR}{EI}\int_\omega^{\pi-\omega}\left[L\cos\omega - R\sin\omega + R\sin(\omega + a)\right]^2 da \tag{23}$$

Total deflection per segment δ_n is just the superposition of δ_r and δ_c,

$$\delta_n = \delta_r + \delta_c \tag{24}$$

For *n* segments the total deflection is

$$\delta_s = n * \delta_n \tag{25}$$

3.3.12 Spring Dimensions

Expressions found for the stress and deflection of the spring can be evaluated for different values of the parameters. Figure 3.3.12.17 presents the results for the deflection of the spring when $F_s = 10$ μN, *t*=3 μm and *T*=28 μm. From then is clear that for the parameters *H*=50 μm, *b*=7 μm and *R*=12 μm, a force of 10 μN, just a third of the admissible force, is enough to deflect one segment of the spring 2 μm. If 3 elements are used to create the spring, the resultant deflection provides more than the required deflection of 4 μm.

Similarly, Figure 3.3.12.18 presents the results for the stress σ, for the same conditions of Figure 3.3.12.17. It is clear from the highlighted value, that the stress is only 19 MPa compared to the admissible value of 122 MPa (Table 3.3.12.2).

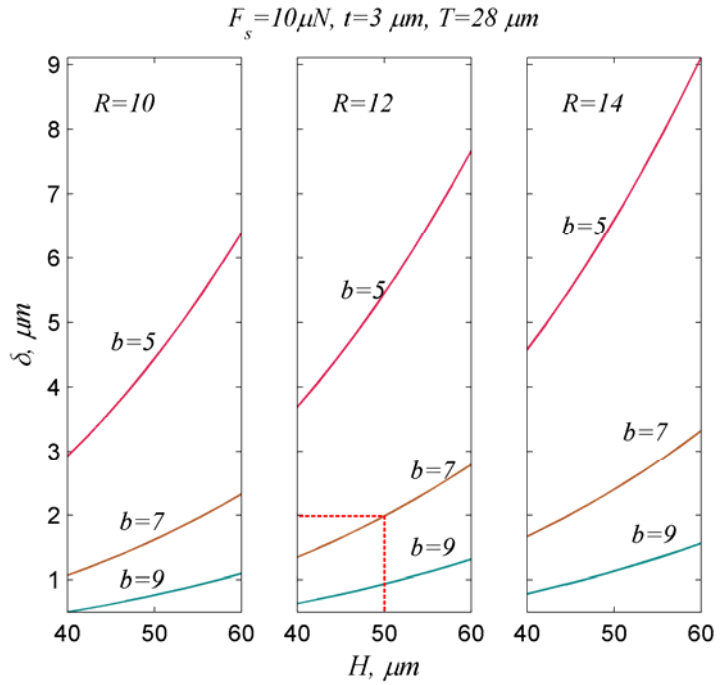

Figure 3.3.12.17. Deflection in the spring.

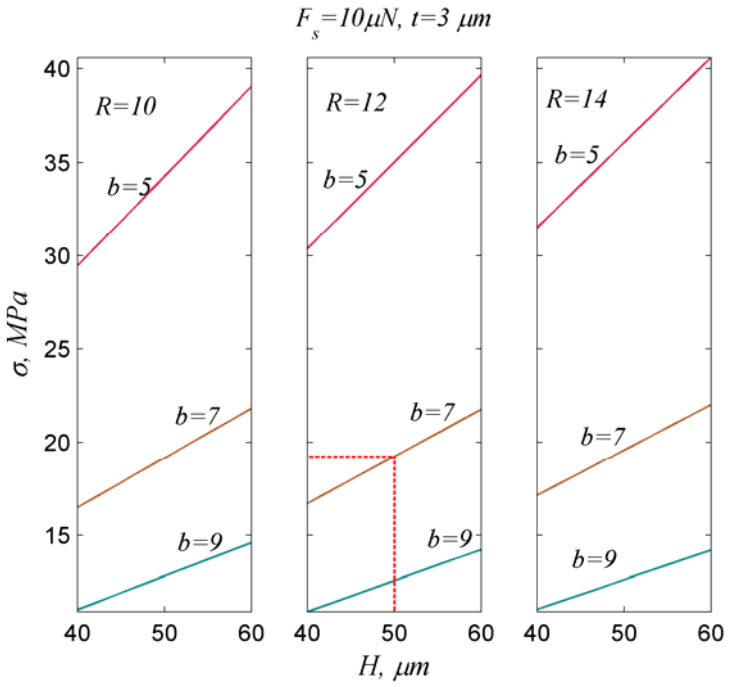

Figure 3.3.12.18. Stress in the spring.

Dimensions found yield a conservative and reliable device. Table 3.12.3 summarizes the results. Some of them are not critical and their calculations were not included.

Table 3.12.3 Main dimensions of the device.

Parameters Beams	Parameters Spring
Length, L_a : 200 µm Width, *w*: 7 µm Thickness of each layer, *t*: 1.5 µm Number of beams: 12 Material beams: aluminum and silicone dioxide	Width, *b*: 7 µm Thickness, *2t*: 3 µm Free length, d_0 : 80 µm *H*: 50 µm *T*: 28 µm *R*: 11.5 µm
Parameters Platform L_p : 120 µm	Parameters resistor Material: chrome Width: 5 µm Thickness: 0.2 µm

3.4 Manufacturing Process

This section presents a sequence to manufacture the device. The device is formed by three materials: silicone dioxide and aluminum for the bimorph beams and between them chrome for the resistor. Processes are common and they do not involve any strange requirements. Some experiments were performed at the University of Florida nanofacilities. The manufacturing process presented here takes advantage of that experience. Five masks are used to define all the features of the system. In the following Figures depth dimensions are magnified to assist in the visualization of the geometry of each step.

The substrate for the device is silicon. The wafer does not require any particular electrical or mechanical properties, and the crystal orientation does not affect the process (Figure 3.4.19).\

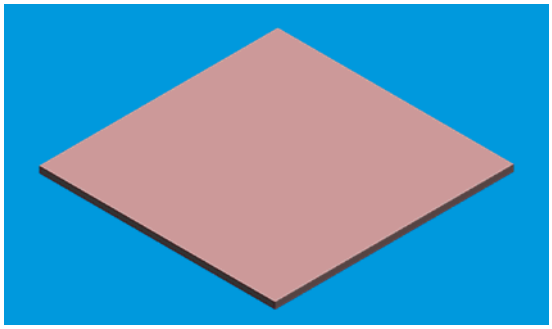

Figure 3.4.19. Silicone substrate.

A first layer of 0.80 µm of silicone dioxide is deposited over the wafer using plasma enhanced chemical vapor deposition (PECVD) process (Figure 3.4.20).

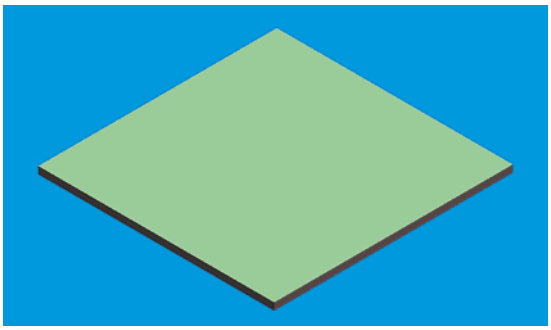

Figure 3.4.20. First layer of silicone dioxide.

Then a layer 0.20 µm of chrome is sputtered over the first silicone dioxide layer (Figure 3.4.21).

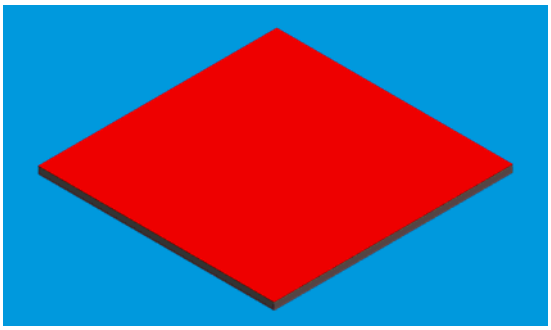

Figure 3.4.21. Layer of chrome.

Using a mask, the chrome is patterned and then plasma etching is used to obtain the shape of the resistor (Figure 3.4.22).

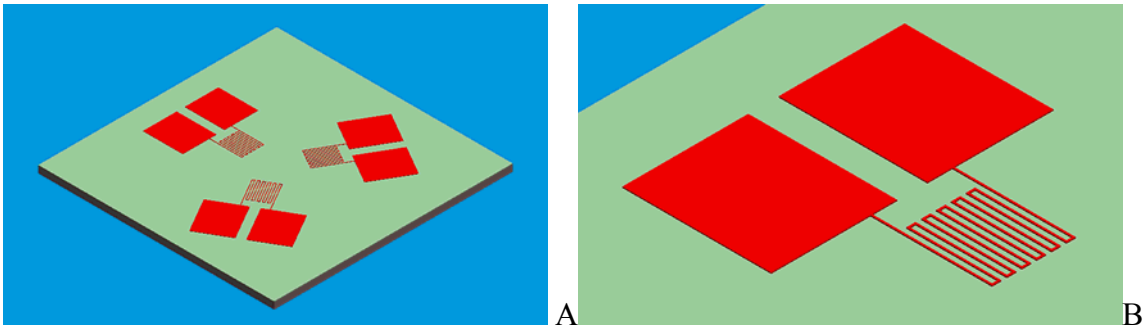

Figure 3.4.22. Resistor. A) General view. B) Detail.

A second layer of silicone dioxide with thickness 0.70 µm is applied using PECVD (Figure 3.4.23A). As a result the resistor is isolated, however it is necessary to open a way to be able to apply voltage (Figure 3.4.23B).

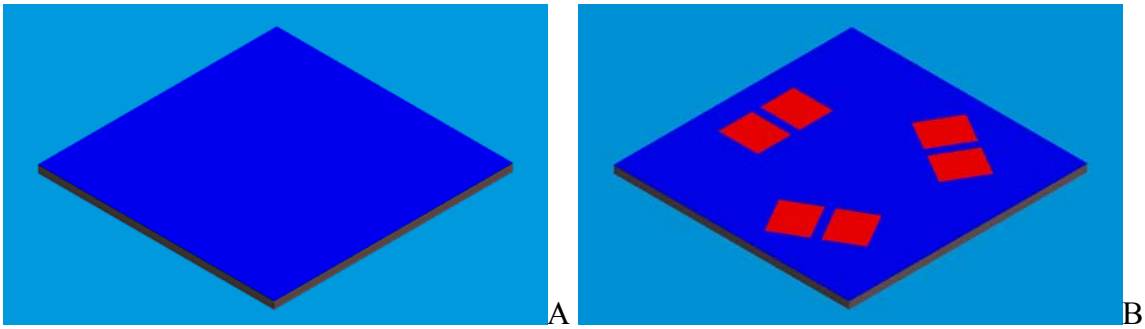

Figure 3.4.23. Second layer of silicone dioxide. A) General view. B) Detail.

Aluminum with thickness of 1.5 µm is sputtered to complete the materials for the device (Figure 3.4.24A). To be able to apply voltage to the resistors it is necessary to create isolated areas called the pads. For this purpose an additional mask is required (Figure 3.4.24B).

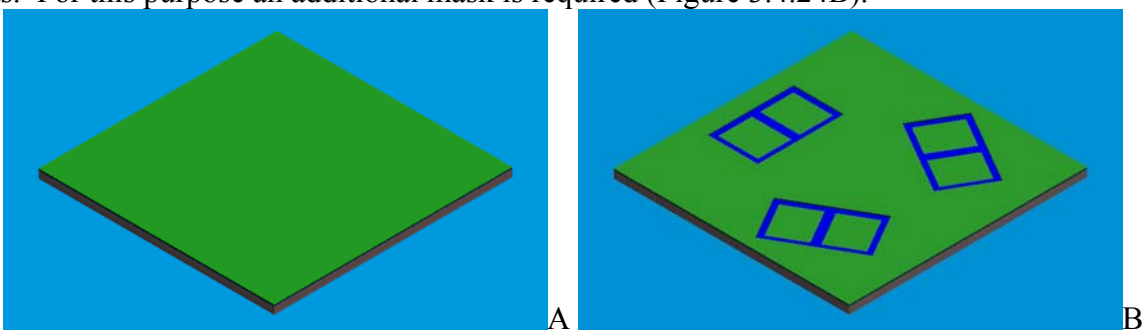

Figure 3.4.24. Aluminum layer. A) General view. B) Detail.

The next step is to obtain the shape of the cantilever beams and the moving platform. A new mask is required to avoid damages in the already created pads. Figure 3.4.25 illustrates the result when the aluminum has been removed and the second layer of silicone dioxide is exposed.

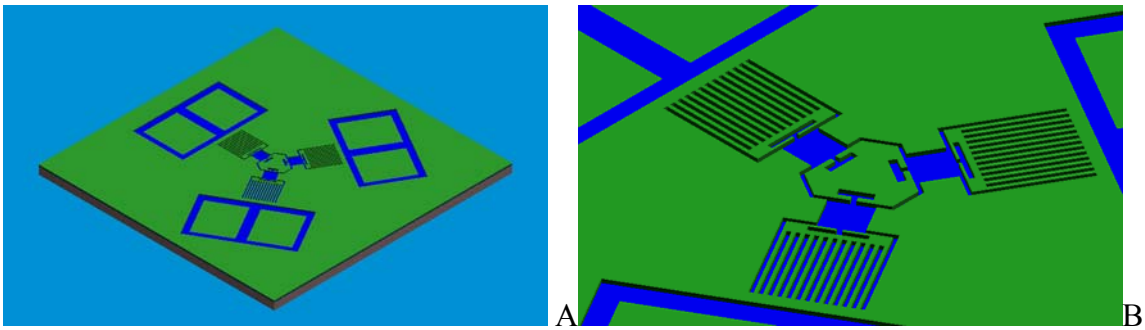

Figure 3.4.25. Etching of areas in the aluminum corresponding to the actuators and platform. A) General view. B) Detail.

The photoresist required for this process is still over the aluminum, but it is not presented to simplify the visualization. Between the central platform and the actuators appear some free areas that will be used for the joints.

A new etching process, but the same mask, is required to remove both layers of silicone dioxide. The process stops when the substrate is reached. At this moment the photoresist is stripped (Figure 3.4.26).

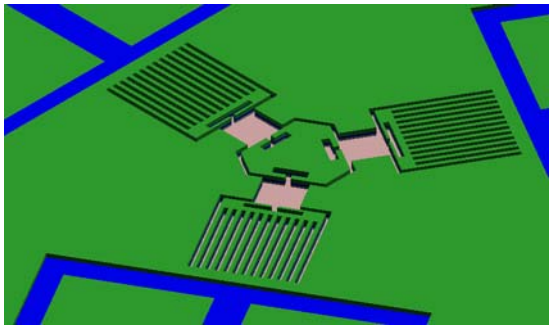

Figure 3.4.26. Etching of silicone dioxide

Springs are created in the next two steps. A layer of polymide is spun on the wafer (Figure 3.4.27).

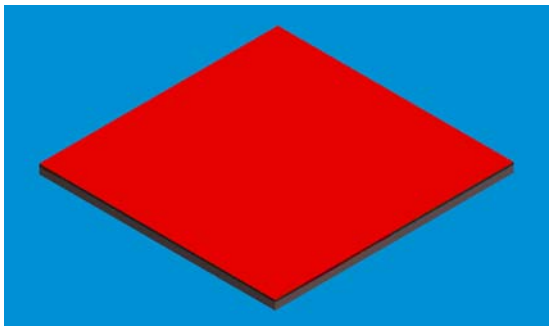

Figure 3.4.27. Polymide layer.

With a mask, the photo definable polyamide is patterned to create the springs. After curing and removing remaining material (Figure 3.4.28).

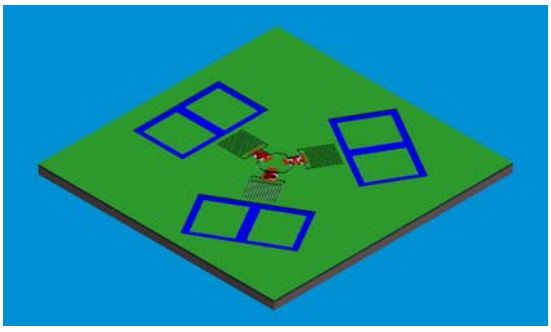
A
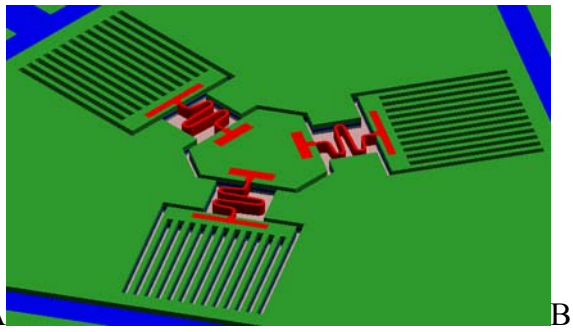
B

Figure 3.4.28. Polyamide springs. A) General view. B) Detail.

The main elements of the mechanisms are ready. The objective of the next steps is to release the beams, springs and platform. A backside etch on the substrate is illustrated in Figure 3.4.29. This step determines the depth of the platform.

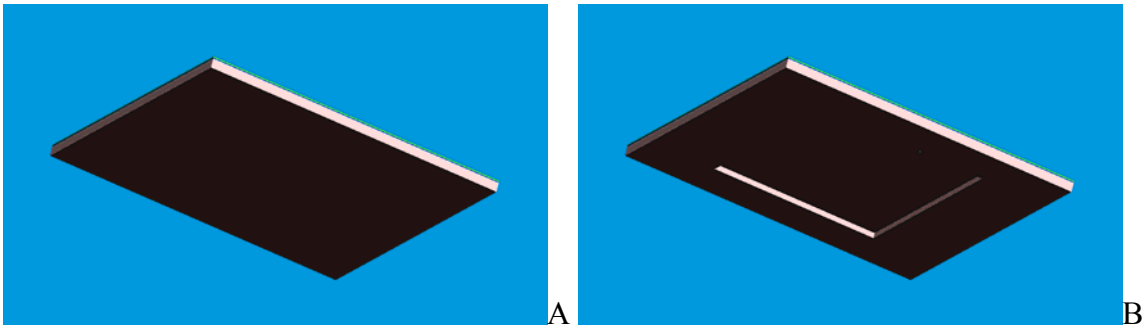
A B

Figure 3.4.29. Backside etch. A) Before etching. B) After etching.

The process continues in the front side. Figure 3.4.30 shows a section view of the wafer and the detail of the substrate under a spring. The substrate material must be removed.

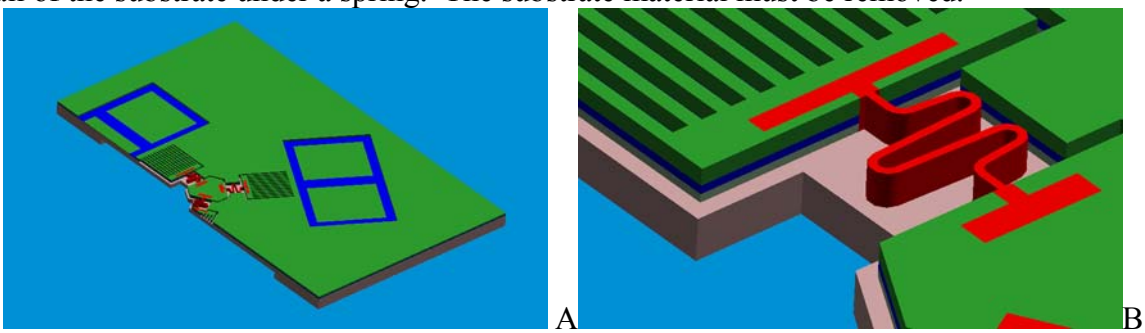
A B

Figure 3.3.4.30. Section view of the device. A) General view. B) Detail.

The exposed parts of the substrate are removed using deep reactive ion plasma etch (Figure 3.4.31). Since the etching process is much more aggressive on silicone than on aluminum or polymide, a new mask is not required. At this moment all the elements are still attached to the wafer by small portions of the substrate.

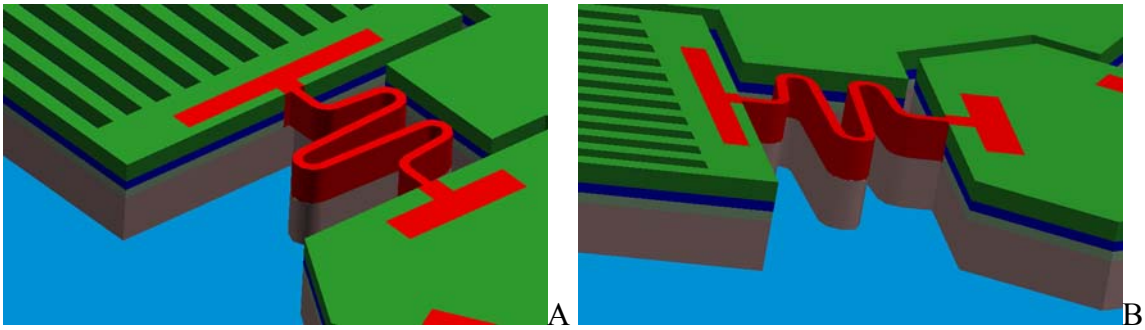
A B

Figure 3.4.31. Deep reactive ion etching. A) General view. B) Detail.

Finally isotropic etching is used to remove the portions under the beams and spring (Figure 3.4.32). Some undercut is also present in the platform, but it does not affect its strength.

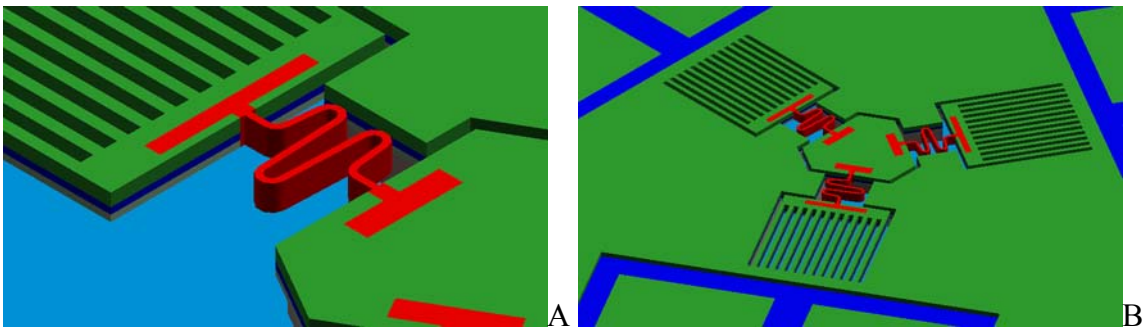
A B
Figure 3.4.32. Isotropic etch. A) General view. B) Detail.

3.5 References

1. Chen,W., Chien, C. Hsieh, J. , and Fang, W., *"A Reliable Single-Layer Out-of-Plane Micromachined Thermal Actuator,"* Sensors and Actuators A, 103(1-2), pp. 48-58, 2003.

2. Milanovic, V., *"Multilevel Beam SOI-MEMS Fabrication and Applications,"* Journal of Microelectromechanical Systems, 13(1), pp 19-30, 2004.

3. Lee,C., *"Design and Fabrication of Epitaxial Silicon Micromirror Devices,"* Sensors and Actuators A, 115, pp 581-590, 2004.

4. Bronson, J.R., and Wiens, G. J., *"Control of Micro Mirrors for High Precision Performance,"* Proceedings of the Florida Conference on Recent Advances in Robotics, Miami, FL, May 2006.

5. Fu Y., Du H., Huang W., and Hu, M., *"TiNi-Based Thin Films in MEMS Applications: a Review,"* Sensors and Actuators A, 112(2-3), pp. 395–408, 2004.

6. Jain, A., Qu, H., Todd, S, Xie, H., *"A Thermal Bimorph Micromirror with Large Bi-directional and Vertical Actuation,"* Sensors and Actuators A, 122(1), pp. 9-15, 2005.

7. Ebefors, T., Mattsson, J., Kalvesten, E. and Stemme, G., "*Robust Micro Conveyer Realized By Arrayed Polymide Joint Actuators,"* Proceedings Twelfth IEEE Conference on Micro Electro Mechanical Systems, Orlando, FL, January 1999 pp. 576-581.

8. Suh, J., Darling, R., Bohringer, K., Donald, B., Baltes, H., and Kovacs, G., *"CMOS Integrated Ciliary Actuator Array as a General-Purpose Micromanipulation Tool for Small Objects,"* Journal of Microelectromechanical Systems, 1999, 8 (4), pp. 483-496.

9. Schweizer, S., Calmes, S., Laudon, M., and Renaud, P., *"Thermally Actuated Optical Microscanner with Large Angle and Low Consumption,"* Sensors and Actuators A, 1999, 76(1-3), pp. 470–477.

10. Jensen K., Howell L., and Lusk K.*"Force Relationships for an XYZ Micromanipulator with Three Translational Degrees of Freedom,"* Proceedings Design Engineering Technical Conferences, ASME, Salt Lake City, Utah, USA, September 2004.

11. Bamberger, H. and Shoham, M., *"Kinematic Structure of a Parallel Robot for MEMS Fabrication,"* Proceedings On Advances in Robot Kinematics, Netherlands, 2004, pp. 113-122.

12. Tung, Y., and Kurabayashi, K., *"A Single-Layer PDMS-on-Silicon Hybrid Microactuator with Multi-Axis Out-Of-Plane Motion Capabilities - Part I: Design and Analysis,"* Journal of Microelectromechanical Systems, 14 (3), 2005, pp. 548-557.

13. Fuller, R., *Synergetics, Explorations in the Geometry of Thinking*, Collier Macmillan, London, 1975.

14. Kenner, H., "*Geodesic Math and How to Use It*," University of California Press, Berkeley, 1976.

15. Calladine, C., *"Buckminster Fuller's Tensegrity Structures and Clerk Maxwell's Rules for the Construction of Stiff Frames,"* Intern'l Journal of Solids and Structures, 1978, 14, pp. 161–172.

16. Murakami, H., *"Static and Dynamic Analyses of Tensegrity Structures. Part 1. Nonlinear Equations of Motion,"* International Journal of Solids and Structures, 38, 2001, pp. 3599-3613.

17. Crane, C., Duffy, J. and Correa, J., *"Static Analysis of Tensegrity Structures,"* Journal of Mechanical Design, **127**(2), 2005, pp. 257-268.

18. Knight, B.F., *"Deployable Antenna Kinematics using Tensegrity Structure Design,"* Ph.D. thesis, University of Florida, Gainesville, FL, 2000.

19. Sultan, C., and Corless, M., *"Tensegrity Flight Simulator,"* Journal of Guidance, Control, and Dynamics, **23**(6), 2000, pp. 1055-1064.

20. Tibert, A., and Pellegrino S., "Deployable Tensegrity Reflectors for Small Satellites," Journal of Spacecraft and Rockets, **39**(5), 2002, pp.701-709.

21. Sultan, C., and Skelton, R., *"A Force and Torque Tensegrity Sensor,"* Sensors and Actuators A, **112**(2-3), 2004, pp. 220–231.

22. Ingber, D. E., *"Cellular Tensegrity: Defining New Rules of Biological Design That Govern the Cytoskeleton,''* Journal of Cell Science, 104, 1993, pp. 613–627.

23. Furuya, H., "Concept of Deployable Tensegrity Structures in space Application," Int. J. Space Struct. **7**(2), 1992 p. 143–151.

24. Sultan, C., and Skelton, R., *"Deployment of Tensegrity Structures,"* International Journal of Solids and Structures 40, 2003, pp. 4637–4657.

25. Pelesko, J. A., and Bernstein, D. H., "*Modeling MEMS and NEMS*," CRC Press, Boca Raton, FL, 2002.

26. Hah, D., Yoon, E., and Hong, S., *"A Low-Voltage Actuated Micromachined Microwave Switch Using Torsion Springs and Leverage,"* IEEE Transactions On Microwave Theory and Techniques, 48 (12), 2000, 2540-2545.

27. Yang, S., Chen, X., Hasegawa, M., and Motojima S.,"*Conformations of Super-Elastic Carbon Micro/Nano-Springs and their Properties,"* Proceedings of the Internt'l Conference on MEMS, NANO and Smart Systems, Alberta, CA, August 2004.

28. Hata, S., Kato, T., Fukushige, T., and Shimokohbe, A., *"Integrated Conical Spring Linear Actuator,"* Microelectronic Engineering 67–68, 2003, pp. 574–581.

29. Senturia, S. D.*Microsystem Design*, Kluwer, Boston, 2001.

30. Boresi, A. P., and Schmidt, R.J., "*Advanced Mechanics of Materials*," Wiley, New York, 2003.

31. Liu, C., "*Foundations of MEMS*," Prentice, Upper Saddle River, NJ, 2006.

32. Crane, C., and Duffy, J., "*Kinematic Analysis of Robot Manipulators*," Cambridge University Press, USA, 1998.